nature electronics

Supplementary information

https://doi.org/10.1038/s41928-025-01374-6

A programmable and self-adaptive ultrasonic wireless implant for personalized chronic pain management

In the format provided by the authors and unedited

Supplementary Information

A programmable and self-adaptive ultrasonic wireless implant for personalized chronic pain management

Content

Supplementary Notes 1-7

Supplementary Figures 1-32

Supplementary Tables 1-5

Supplementary References

Supplementary Note 1. Device piezoelectricity

To realize the electrical stimulation for chronic pain management, the direct and in-direct piezoelectric effects were applied during the utilization of the ultrasound-induced wireless implantable (UIWI) Stimulator and wearable ultrasound transmitter (WUT). The indirect piezoelectric effect occurred in the WUT. The input voltage generated from the function generator and amplified by RF amplifier was utilized to drive the WUT. The piezoelectric material of the WUT is subjected to the electric field in the polarization direction, causing the periodic mechanical deformation (at a frequency consistent with the input electrical signal) and transmitting the ultrasound wave as a mechanical force [1,2]. This process is converting electric energy into mechanical energy. Afterwards, the propagated ultrasound penetrated through the tissue and directly hit the surface of the piezo-element in UIWI stimulator, causing periodic mechanical deformation (at a frequency consistent with the ultrasound) of the piezo-element. When the structure of the piezo-element was mechanically deformed, induced charges emerged on the top and bottom electrodes. The induced charges flow through the external structure equalizes the resulting piezoelectric field. The charges move through the connected external circuit. Hence, the UIWI stimulator is wirelessly powered by ultrasound emitted by WUT and this UIWI device called ultrasonic wireless implant. Finally, the ultrasonic energy is converted into an output of piezoelectric potential by the UIWI stimulator, leading the electrodes to achieving electrical stimulation inside the spinal cord to realize personalized chronic pain management.

Supplementary Note 2. Characterization of piezo-element

To characterize the performance of the piezoelectric composite element, the electromechanical coupling coefficient (k_t), piezoelectric coefficient (d_{33}), and voltage coefficient (g_{33}) were measured and calculated. d_{33} of the piezomaterial illustrates the relationship between polarization and stress at constant field, which can be measured directly by d_{33} meter (YE2730A, APC international, Ltd., Mackeyville, PA, USA) [3]. k_t represents the conversion efficiency between electrical and acoustic energy in piezo-element, which can be determined by following equation [4],

$$k_t = \sqrt{\frac{\pi f_r}{2f_a} \times cot\frac{\pi f_r}{2f_a}} \quad (1)$$

where f_r and f_a is resonant frequency and anti-resonant frequency of the tested piezo-element. And they were determined by Impedance analyzer (Agilent 4294A, Santa Clara, CA, USA). Besides, the g_{33}, illustrating the sensitivity of the piezocomposite to sense ultrasound, can be calculated as [5],

$$g_{33} = \frac{d_{33}}{\varepsilon_{33}^T} \quad (2)$$

Where ε^T_{33} is the relative dielectric Constant, and it can be described as [5],

$$\frac{\varepsilon_{33}^T}{\varepsilon_0} = \frac{C^T h}{\varepsilon_0 A} \quad (3)$$

Where C^T is the capacitance of the piezo-element, h is the thickness of the piezo-element, and A is the area of the piezo-element. The capacitance and dielectric loss were characterized by 1715 LCR Digibridge (QuadTech, CA, USA). All the parameters and calculated results of the fabricated piezo-element are listed in **Supplementary Table 2**.

To calculate the energy efficiency of the UIWI stimulator, two parts of the power will be considered. First, the transmitted acoustic power from wearable ultrasound transmitter will be considered. The acoustic power (P_a) was computed as the integration of acoustic intensity in area based on the hydrophone mapping result (**Supplementary Fig. 15**). Second, the received electrical power will be calculated by the converted electrical voltage as $P_r = (U^2/R) *$ duty cycle. Hence, the efficiency can be demonstrated as P_r/P_a. In the study, the power conversion efficiency of the UIWI stimulator device under the working condition (Input of 1 -10 V for wearable ultrasound transmitter) achieved 3.57%.

Supplementary Note 3. The discussion of the electrodes in the UIWI stimulator

To demonstrate the potential long-term usage of the UIWI stimulator, accelerated lifetime testing (ALT) was applied to characterize the post-implantation performance of the electrode in UIWI stimulator. ALT can effectively shorten the testing cycle while mimicking the in-body environment after implantation. We performed ALT on our fabricated device to provide a better understanding of the underly factors that can cause implant failure or complications. According to the Arrhenius modeling of reaction acceleration, the 'aging factor' can be determined using the equation below:

$$Aging\ factor = Q_{10}^{\frac{T_{accelerated} - T_{target}}{10}} \quad (4)$$

Where it is common to use 2 for Q_{10} and in our case, $T_{\text{accelerated}}$ is 70 degrees Celsius and T_{target} is 37 degrees Celsius[6]. An 10x acceleration factor can be calculated for our study.

Electrochemical impedance spectroscopy (EIS) and high-resolution imaging was used to characterize electrode stability during ALT. The mean-time-to-failure (MTTF) was determined when the measured 1 kHz impedance of the samples changed over 25% of the initial value [7]. As shown in **Supplementary Fig. 7a - b**, we have identified the device to reach failure point at day 3. This result corresponds to device failure after 30 days post-implantation. The high-resolution microscope image shown in **Supplementary Fig. 7c** also indicates fluid leaking into the polyimide-polyimide interface, impairing electrode integrity. Therefore, even though the device has shown potential for long-term usage, much more work needs to be done to optimize the stability of the polymer-to-polymer and polymer-to-metal interfaces. As a result, for future work, we plan on investigating ways to improve interfacial adhesion as mentioned above. Much work has been done on this field, and we hypothesize if we adopt those methods, we will see a more enhanced long-term stability performance. Specifically, we plan on adding an oxygen plasma treatment step on the polyimide films as well as using silicon carbide as an adhesion layer for our future device studies[8,9]. Besides, it should be noted that the proposed prototype works under voltage mode, which could have negative impacts on safety and electrode longevity. In future iterations of our device design, we will also plan to incorporate application specific integrated circuit (ASIC) consisting of power management, control, and stimulation modules that will enable stable biphasic current output based on the varying neural impedance. This aspect of current-controlled biphasic stimulation with improved electrodes by ultrasound-induced wireless implant device will be a focal point of our subsequent research efforts for future translational studies.

Supplementary Note 4. Acoustic pressure & intensity and Mechanical index calculation

WUT was applied to transmit the ultrasonic energy to hit the piezo-element of the UIWI stimulator to convert the ultrasound into electrical stimulus signal. To ensure the transmitting ultrasonic energy under the FDA proved standard, the hydrophone was utilized to measure and calibrate the acoustic/ultrasonic energy from WUT. Hydrophone probe is a sensitive ultrasound transducer that converts received acoustic pressure from exciting probe into electrical voltage signals [10,11]. And it is capable of sensing acoustic wave over a broad range of frequencies with high spatial resolution. The recorded voltage can correspond to specific acoustic pressure based on the hydrophone's sensitivity curve, which is already calibrated by manufacture [12,13]. Thus, the acoustic peak negative pressure (P_{peak-}) from the WUT can be calculated and determined by following equation [13],

$$P_{peak-} = \frac{V_{peak-}}{Senstivity} \tag{5}$$

where V_{peak-} is the peak negative voltage. Afterwards, the Mechanical Index is calculated by the following equation [14]:

$$MI = \frac{P_{peak-}}{\sqrt{f_c}} \tag{6}$$

where f_c is the central frequency of the WUT. Moreover, to calculate the spatial-peak-pulse average intensity (I_{sppa}), the following equation is shown [15],

$$I_{sppa} = \frac{P_{peak-}^2}{2 \times \rho \times C} \tag{7}$$

Where ρ is the background density (DI-water), C is the acoustic velocity in background (DI-Water). Based on the Duty cycle,

$$Duty\ cycle = PD \times PRF \tag{8}$$

where PD is pulse-duration, and PRF is pulse repetition frequency. Hence the spatial peak temporal average intensity (I_{spta}) can be calculated as,

$$I_{spta} = I_{sppa} \times Duty\ cycle \tag{9}$$

Hence, the acoustic pressure and intensity of the WUT under different input voltage can be calculated and determined. The calculated results are listed in **Supplementary Table 4.**

Supplementary Notes 5. Ultrasound response on spinal cord during pain management

To explore the direct effects of ultrasound stimulation on spinal nerve activity, we conducted a series of experiments to determine whether ultrasound stimulation could enhance or inhibit signal conduction within the spinal nerves. Given that the animals were under anesthesia, there was minimal conduction of motor neural signals. Previous studies have attempted to induce changes in muscle potentials in the legs by directly electrically stimulating the motor cortex of the brain. Herein, in **Supplementary Fig. 24**, we selected direct electrical stimulation of the spinal nerves to induce motor potentials in the legs, implementing electrical stimulation between the T11 and T12 vertebrae using screws. This setup allowed us to adjust the amplitude of the induced electrical stimulation, thereby inducing varying response levels. Without removing the bone of the spinal cord, 1 MHz ultrasound stimulation was then applied to the L4-L5 segment and recorded electromyography (EMG) signals from both the left and right legs. Our data acquisition system facilitated real-time control of the electrical stimulation.'

The parameters for electrical stimulation were derived from existing literature and followed established protocols, with a frequency of 100 Hz and pulses repeated 10 times with 5-second intervals. In contrast, ultrasound stimulation was administered with shorter 1-second intervals and a burst duration of 300 ms (30% - duty cycle), while EMG signals were simultaneously recorded[16-21]. An initial electrical stimulation of 0.08 mA was applied, repeated ten times, as this was the minimum current required to establish a stable potential. We explored three different ultrasound stimulation intensities to assess the impact of ultrasound intensity (**Supplementary Fig. 25**). It was observed that at an ultrasound intensity of 2.8 MPa, the potentials remained unchanged. Increasing the ultrasound stimulation intensity to 3.3 MPa resulted in noticeable differences in both maximum and average peak values. At an extremely high stimulation intensity of 3.8 MPa, peak values were significantly inhibited, but the potentials were not completely suppressed.

In summary, the high-intensity US stimulation may partially obstruct neural signal transmission in spinal nerves, but does not completely inhibit signaling. Note that, in our study, the ultrasound stimulation intensities (acoustic intensity) used was below 2.8 MPa, which illustrated that our applied ultrasound energy from WUT did not adversely affect signal transmission during pain management.

Supplementary Note 6. Sample entropy

Entropy is a fundamental thermodynamics concept widely used in analyzing various physical signals, including electrophysiological signal [22-24]. Entropy is a valuable tool for assessing the randomness and predictability of a system. Recent investigations have focused on applying entropy to investigate EEG under different conditions and in various neurological disorders [25-28]. Herein, our study aims to compare different entropy indices with other physiological indicators and examine the applications of entropy in diverse physiological contexts.

The electrophysiological signal data points *x(n)* ranges from 1 to the length of the time series data *N*. The data length in the study is each 0.5 seconds as a time series to analyze the data with a 40 kHz sampling frequency record as a cycle to complete a Sample Entropy (*SE*) calculation [29]. Consequently, define two vectors: *x(n)=x(i)*, where *i* = 1, 2,…, *N*. At first, *X(1)* to *X(N-m+1)*, can be defined as [30],

$$X(i)=[x(i),\ x(i+1),\ldots,x(i+m-1)] \tag{10}$$

Where *m* represents the embedding dimension, which determines the data patterns' length. The comparison process, *X(i)* and *X(j)*, examines the relationship between the template and adjacent data points. The extent of regularity or irregularity within the time series can be assessed by evaluating the similarity or dissimilarity between consecutive data points. This analysis allows for the detection of patterns and dependencies between neighboring data points, providing insights into the complexity and underlying dynamics of the time series. *X(j)* time series can be defined in the time series as [30],

$$X(j)=[x(j),\ x(j+1),\ldots,x(j+m-1)] \tag{11}$$

The distance, *d[X(i), X(j)]*, pertaining to vectors *X(i)* and *X(j)*, is precisely characterized as the

$$d[X(i),X(j)]=\max_{k=0,\ m-1}[/x(i+k)-x(j+k)/] \tag{12}$$

maximum absolute difference observed among their respective scalar components.
To calculate the SE, the template vector of possible vectors, $B_i^m(r)$, can be calculated as [30],

$$B_i^m(r)=\frac{1}{N-m-1}\sum_{j=1,j\neq i}^{N-m}V^m \tag{13}$$

where V^m represents the number of distances when *d[X(i), X(j)]* ≤ r and *m=m+1*. And all the template vectors can be added by following the equation [30],

$$B^m(r)=\frac{1}{N-m}\sum_{i=1}^{N-m}B_i^m(r) \tag{14}$$

r is the tolerance level, indicating the maximum acceptable difference between data points. The same methodology is established by calculating the model vector, $A_i^m(r)$, as follows [30],

$$A_i^m(r)=\frac{1}{N-m-1}\sum_{j=1,j\neq i}^{N-m} V^{m+1} \tag{15}$$

furthermore, it can be inferred as follows [30],

$$A^m(r)=\frac{1}{N-m}\sum_{i=1}^{N-m} A_i^m(r) \tag{16}$$

hence, the SE can be calculated as [30],

$$SE(m,r,N)= -\log\frac{A^m(r)}{B^m(r)}=-\log\left[\frac{\sum_{i=1}^{N-m}\sum_{j=1,j\neq i}^{N-m} V^{m+1}}{\sum_{i=1}^{N-m}\sum_{j=1,j\neq i}^{N-m} V^{m}}\right] \tag{17}$$

In this investigation, we computed entropy measures for individual rats in order to evaluate the effects of pain stimuli. Serving as a credible metric, entropy reliably confirmed that the administered pain was substantial enough to induce alterations in the rats' physiological responses, which can be subsequently correlated with other relevant indices in our analysis.

Supplementary Note 7. Future design of the WUT

For current chronic pain management system, the WUT based on cable-connected power supply seems bulky and tedious. To further demonstrate the feasibility of applied WUT for potential long-term operation, the future direction of the advanced WUT will be planned and designed to achieve an untethered system for chronic pain management in the future. And the battery size that can be assembled with WUT for 2-3 days operation will be estimated based on the stimulation modes for treating the general chronic pain symptom.

In future design of the wireless WUT, extreme pain symptom treatment will be considered as example for battery calculation as extreme stimulation mode will cost more power consumption compared to other two pain symptoms (moderate pain and slight pain models). The generation of extreme stimulation mode for treating extreme pain symptoms needs at least effective power of 4mW (based on the driving voltage of 2 V_{pp}, cycle of 1000, interval of 5ms, 15 min duration for one treatment). To replace the functional generator and amplifier, a customized PCB (**Supplementary Figure 31**) is designed and lay out and will be fabricated in the future for connecting the WUT as wireless device. In the design, it contains a Bluetooth part (for remote control) and Direct Digital Synthesis (DDS) part (for sin wave formation), and a power module part (for power supplying both Bluetooth and DDS). Normally, a lower energy Bluetooth has power consumption about 30 - 40mW (nRF52840, Nordic semiconductor, Trondheim, Norway), a common DDS requires a power consumption of 100mW (AD9850, Analog Devices, Wilmington, MA, USA), and a typical power module achieved a conversion efficiency of 80% (LM2596, Texas Instruments, TX, USA). Thus, to supply the wireless WUT for one-time extreme pain symptom treatment, the total power needs from Li-ion battery will be approximately 200mW. For patient with chronic pain, the treatment frequency will be one stimulation treatment per hour [31,32]. Thus, the required energy for 2-day operation can be calculated and estimated as below:

$$\textit{Required energy} = \textit{Power} \times \textit{time} \tag{18}$$

Based on the reference [33-39], a typical energy density of lithium-ion battery is about 400 Wh/L. Hence, the battery volume can be estimated as,

$$\textit{Battery volume} = \textit{Required energy} / \textit{Energy density} \tag{19}$$

Therefore, to achieve a two-day operation for wireless/untethered WUT, the lithium-ion battery will require an approximate volume of 6 cm^3, which can be manufactured approximately as 3.5cm × 3.5cm × 0.5cm as an acceptable size for wearability. However, based on the battery volume estimation, current battery technology may still face challenges in producing smaller battery sizes. In the next step, power management will be optimized to reduce overall consumption. Additionally, hybrid power solutions, such as combining with energy harvesting will be explored to further reduce the overall battery size for untethered operation of the WUT [40-42].

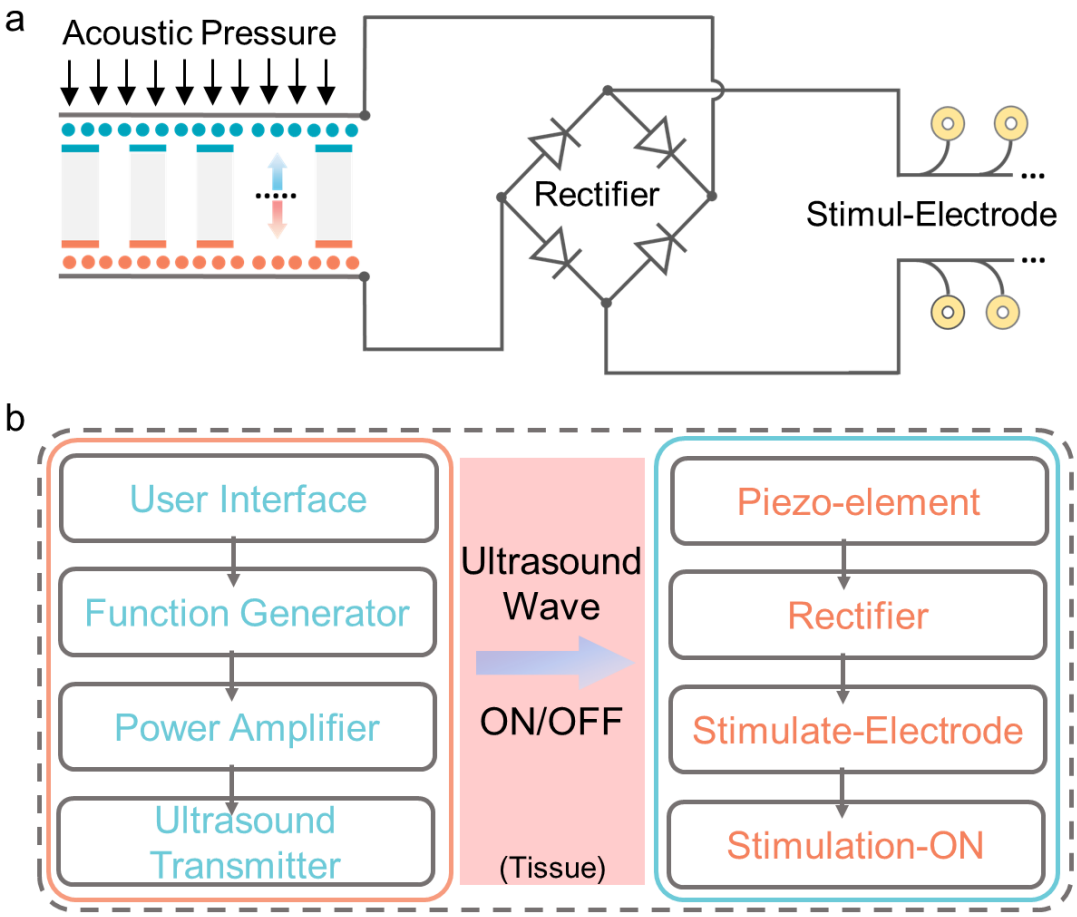

Supplementary Figure 1. Design of UIWI stimulator. a The circuit diagram of the UIWI stimulator. **b** The diagram of the working structure for UIWI stimulator.

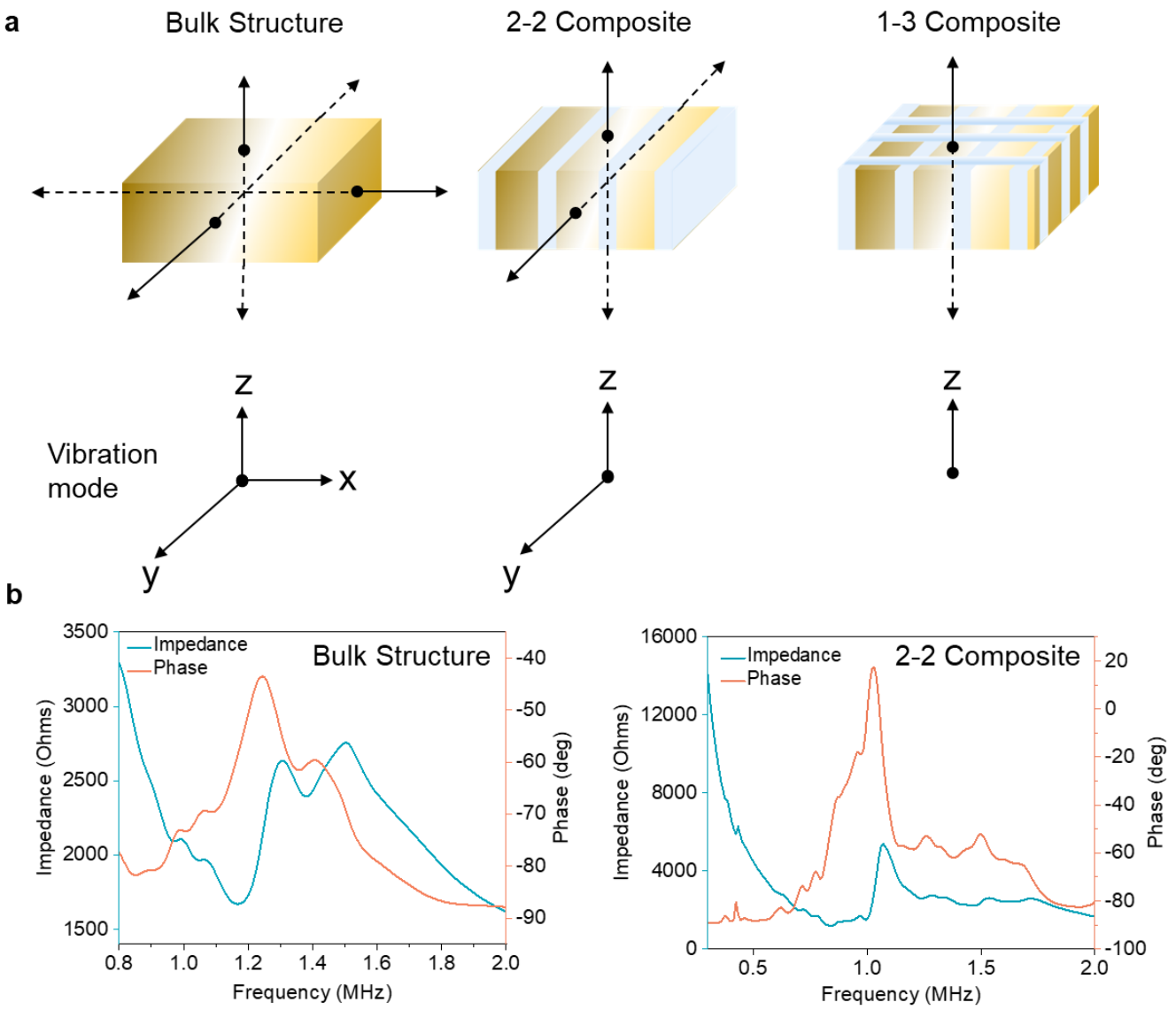

Supplementary Figure 2. Vibration modes and electrical impedance and phase spectrum of three different piezoelectric materials. a Vibration mode of three types of structures (bulk structure, 2-2 composite structures, and 1-3 composite structures). **b** The electrical impedance and phase spectrum of bulk and 2-2 composite structures. The results show that bulk structure has a k_t of 0.47, and 2-2 composite has a k_t of 0.58, and 1-3 composite structure has the highest k_t of 0.63 through suppressing transverse vibration.

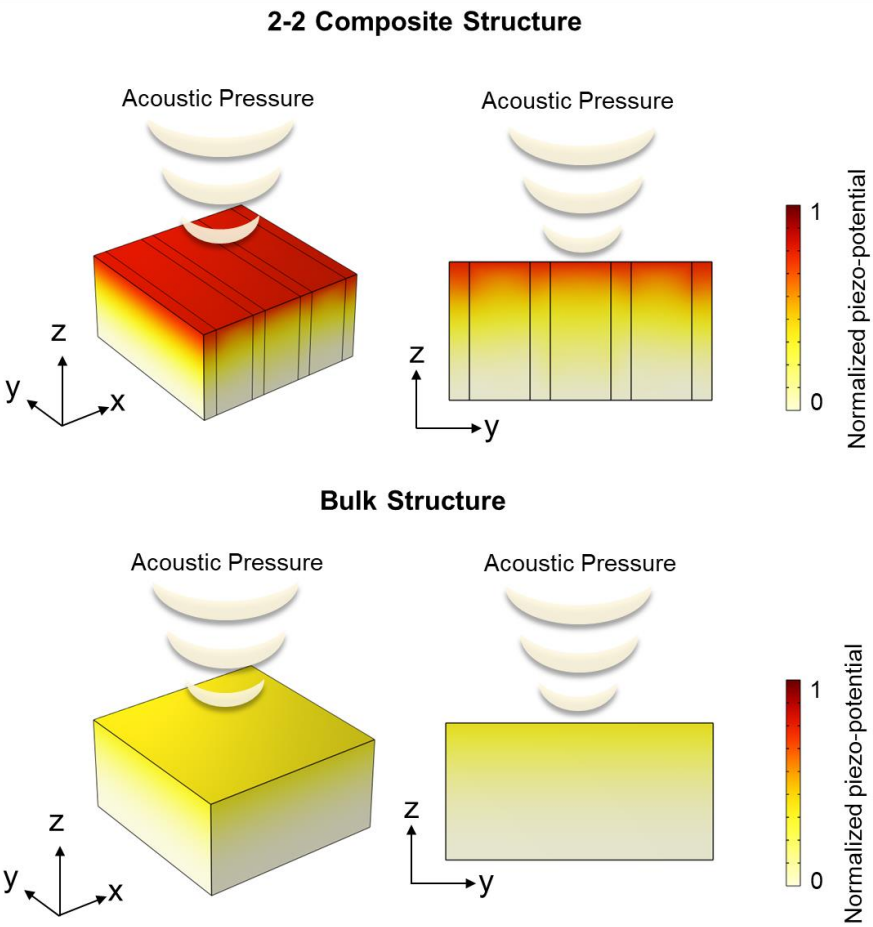

Supplementary Figure 3. Simulations of the different piezo-elements. Simulated piezoelectric potentials inside PZT piezo-elements with 2-2 composite and bulk structures induced by the same acoustic pressure (1 MPa). Element dimension of two structures, 2 mm × 2 mm × 1 mm.

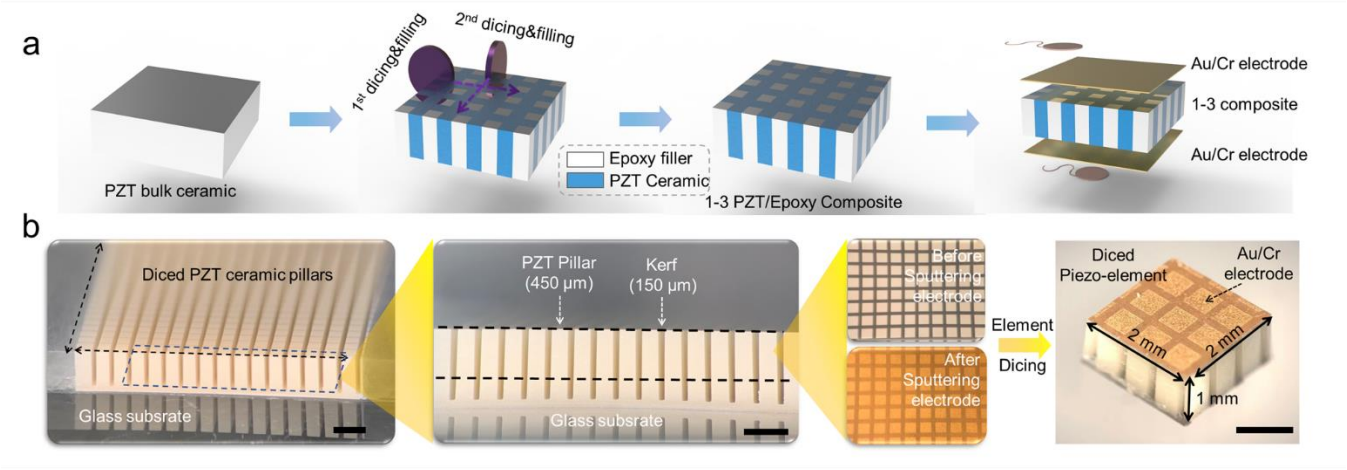

Supplementary Figure 4. The fabrication of the 1-3 PZT/Epoxy composite for UIWI stimulator. a Schematic diagram of the preparation process for the 1-3 PZT/Epoxy composite and piezo-element for UIWI stimulator by applying dicing-and-filling technology. **b** Optical images of the preparation for 1-3 PZT/Epoxy composite and the prepared piezo-element for integration of UIWI stimulator. The prepared 1-3 composite achieves pillar width of 450 μm and kerf of 150 μm, with a volume fraction of 56.25%. After sputtering the Au/Cr (100 nm / 50 nm) electrodes, the single piezo-element (2 mm × 2 mm × 1 mm) for UIWI stimulator was diced. Scale bars, 1 mm.

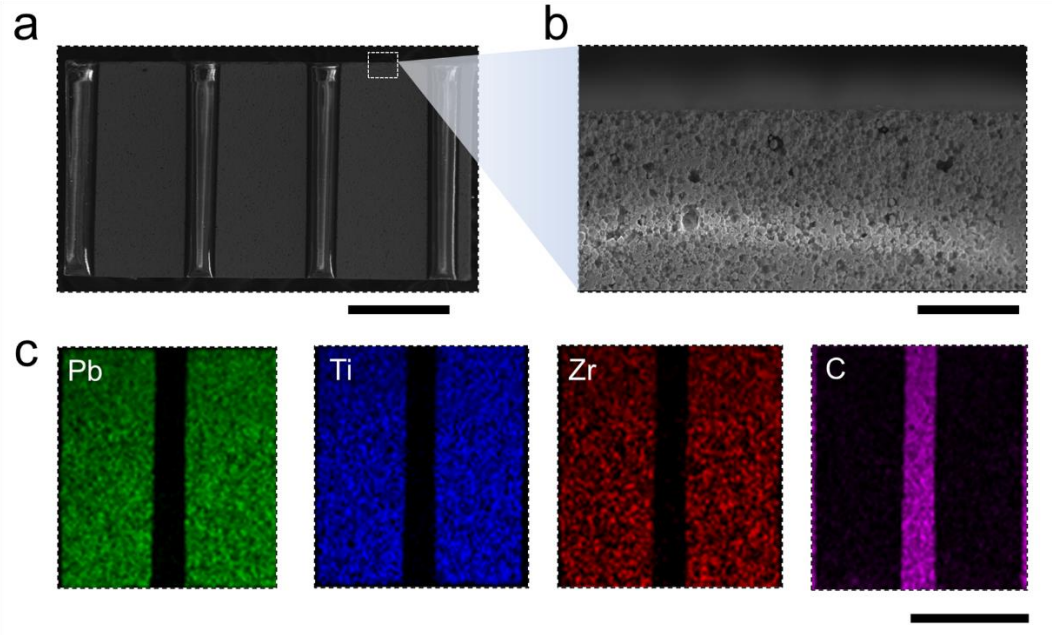

Supplementary Figure 5. Micro-scale characterization of fabricated 1-3 PZT/Epoxy composite element. a A Scanning electron microscope (SEM) image of the prepared piezo-element with 1-3 composite structure. Scale bar, 0.5 mm. **b** A zoom-in SEM image of the prepared piezo-element. Scale bar, 50 µm. **c** Energy dispersive spectroscopy (EDS) elemental mapping of the fabricated piezo-element with composite structure. Scale bar, 600 µm.

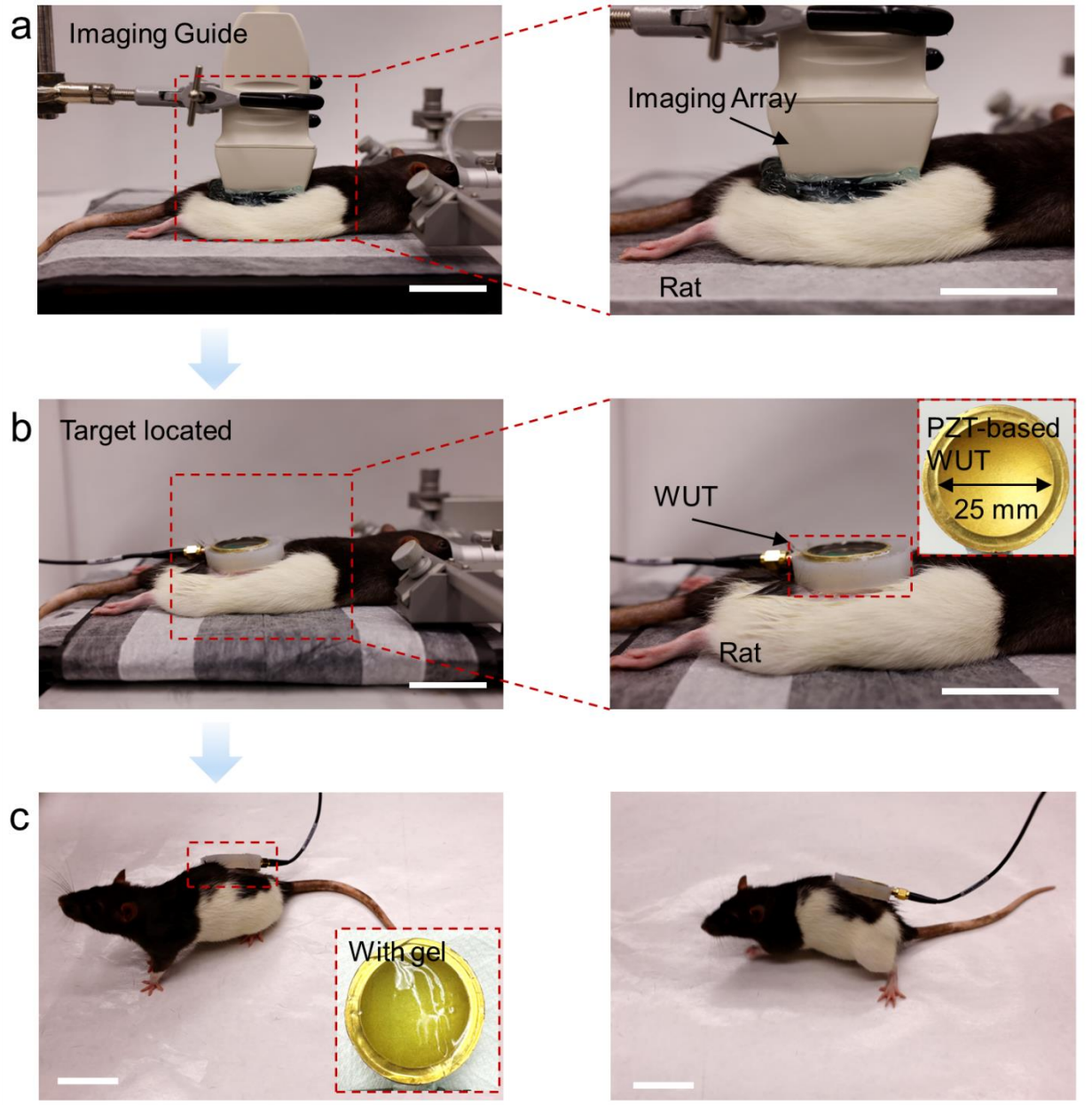

Supplementary Figure 6. WUT and UIWI stimulator alignment. a Ultrasound imaging guidance for locating the implanted UIWI stimulator. **b** WUT patched on the rat after locating the UIWI stimulator, and the WUT without ultrasound coupling gel. **c** Free movement of the rat with WUT, and the WUT with the ultrasound coupling gel. Scale bars, 4 cm.

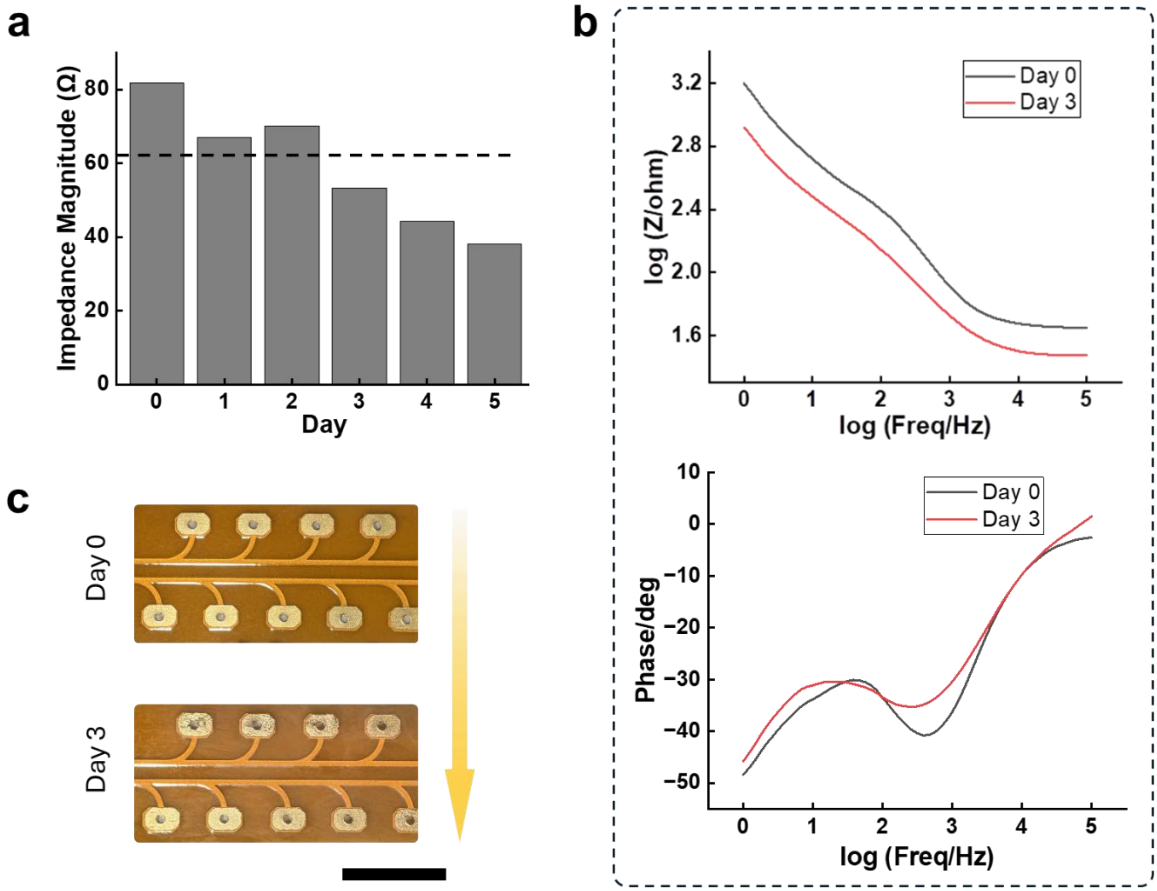

Supplementary Figure 7. Accelerated lifetime testing. a. Impedance magnitude changes at 1 kHz during 5-day period. Dotted line represents threshold for electrode failure. **b**. Impedance response for electrode of the UIWI stimulator. **c**. Optical microscopy images of the electrode at day 1 and day 3. Scale bar, 4 mm.

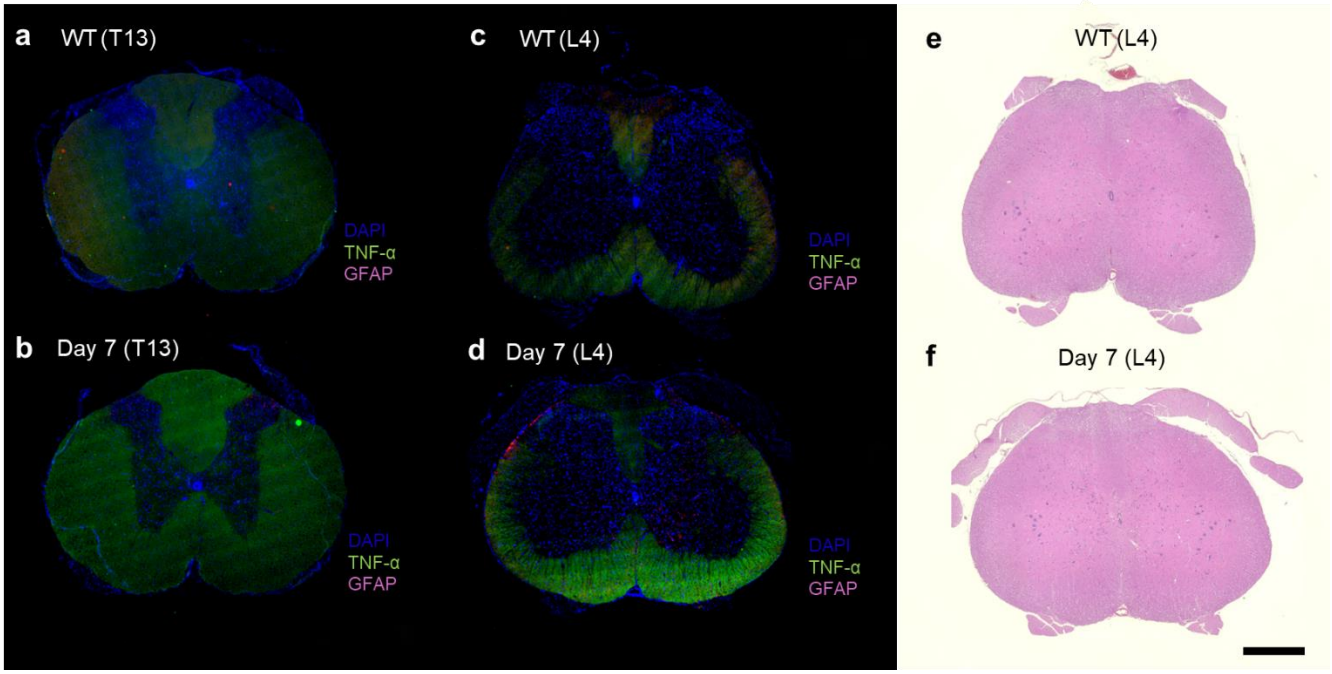

Supplementary Figure 8. Biocompatibility studies for the fully implantable UIWI stimulator on rat. a Immunofluorescence Staining of wild type (WT) Group at T13: The blue fluorescence represents DAPI, which labels cell nuclei; The magenta fluorescence represents GFAP, which labels inflammatory factors; The green fluorescence represents TNF-α, which labels astrocytes. **b** Experimental Group at T13. **c** WT Group at L4. **d** Experimental Group at L4. **e** H&E staining of the WT group at L4. **f** H&E staining of the Experimental Group at L4. Scale bar, 500 μm.

To demonstrate the safety of the implanted device and ensure it does not induce spinal cord inflammatory responses, we performed perfusions on wild type rats as control group and experimental groups of rats which is 7 days post-implantation. Spinal cord tissues were extracted, sectioned, and subjected to immunofluorescence staining. Detailed staining protocols are as follows:

Rats underwent cardiac perfusion, after perfusion, the spinal cord was isolated and placed in 4% paraformaldehyde fixative solution. Once the tissue was sufficiently softened, it was embedded in paraffin for sectioning. After deparaffinization, the buffer (R-universal epitope buffer #NC0752579) and slices were placed in a container (189 mL water, 21 mL 10X buffer for every 2 slides), then the container was placed in a pressure cooker at 100°C for 5 minutes, and then allowed to cool for 1 hour. The samples were then washed 3 times with 1X PBS. The slices were permeabilized using a solution of 0.3% Triton X-100 in PBS with 10% serum from the secondary antibody host species (Donkey Serum, DS, #56-646-05ML) for one hour at room temperature. Following permeabilization, the sections were rinsed thrice in PBS.

1. TNF-α Staining

During spinal cord infection or injury, immune cells release TNFα, a cytokine that can trigger a series of inflammatory responses, such as increased vascular permeability, release of other pro-inflammatory cytokines (e.g., IL-1, IL-6), and recruitment of leukocytes. The expression level of TNFα typically increases in cases of spinal cord inflammation or infection. Immunohistochemical

staining can detect the distribution of TNFα in the spinal cord, aiding in the assessment of inflammatory responses.

Primary antibodies were diluted in a solution of 2.5% DS in PBS, specifically using mouse anti-rat at a dilution of 1:100 (Rabbit anti-rat, Novus Biologicals™ Catalog No. NBP119532SS), and the sections were incubated at room temperature overnight. Post-incubation, the sections were washed three times with PBS containing 0.1% Triton X-100 (PBST). Secondary antibodies were then prepared in PBS, using anti-rabbit 488 at a dilution of 1:1000 (Invitrogen, A-21206). Sections were rinsed on a shaker in 0.1% PBST three times for 30 minutes each. Nuclear staining was performed by adding DAPI diluted between 10,000 to 50,000 times in PBS for 30 minutes. After nuclear staining, sections were washed three times with PBS for 30 minutes each rinse. Finally, the sections were mounted for microscopic examination.

2. GFAP Staining

In cases of inflammation or injury, astrocytes become activated and proliferate, significantly increasing the expression of GFAP. Reactive astrogliosis helps to limit the damage area, but excessive gliosis may lead to scar formation, further impacting neural function. GFAP immunostaining can evaluate the activation status of astrocytes in the spinal cord, which is crucial for assessing the presence of inflammation or injury.

Post-staining results showed that there were no significant differences in TNFα and GFAP expression between the WT group and the experimental group, illustrating the expected potential biocompatibility.

Primary antibody: GFAP at a dilution of 1:100 (Catalog No. #3670, Cell Signaling Technology, Danvers, MA). Secondary antibody: Goat anti-Mouse IgG (H+L), Alexa Fluor™ 647 at a dilution of 1:1000 (Invitrogen, Catalog No. A-21235, USA).

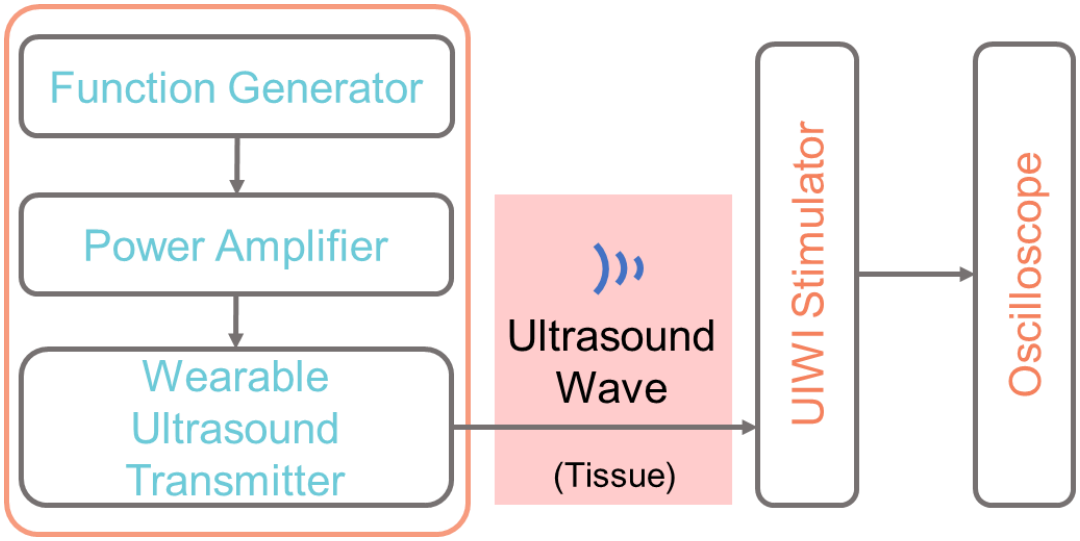

Supplementary Figure 9. Schematic diagram of output test platform for implanted UIWI stimulator. After alignment of the WUT and UIWI stimulator, the degassed ultrasound gel (EcoVue US Gel, HR Pharmaceuticals, Inc.), the coupling medium, was applied on the rat tissue for propagating the ultrasound wave. The driving input voltage of the WUT was generated by function generator and then amplified by a power amplifier. The oscilloscope was applied to measure the output voltages from the UIWI stimulator.

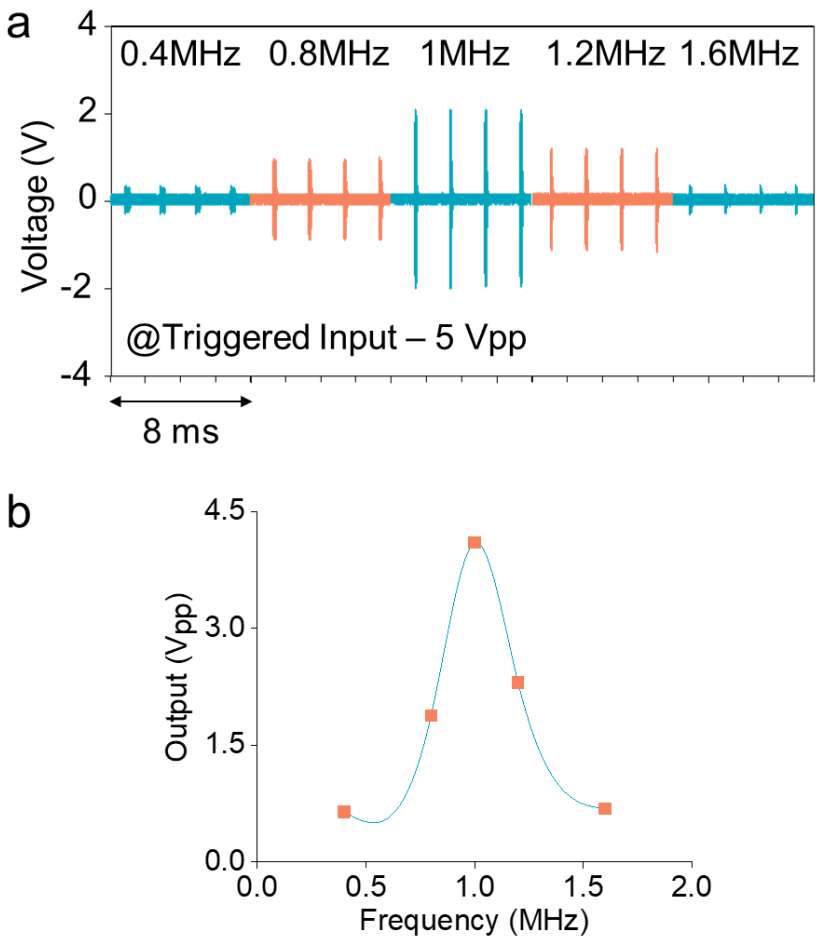

Supplementary Figure 10. Output of the UIWI stimulator with different driving frequencies. **a** Waveforms of the outputs of the UIWI stimulator under frequency from 0.4 MHz to 1.6 MHz. Interval time – 2 ms, Duty cycle – 5 %. **b** The tendency of the output under different frequency (0.4 MHz – 1.6 MHz). It illustrates that UIWI stimulator has demonstrates the highest output under 1 MHz (resonant frequency between WUT and piezo-receiver of UIWI stimulator).

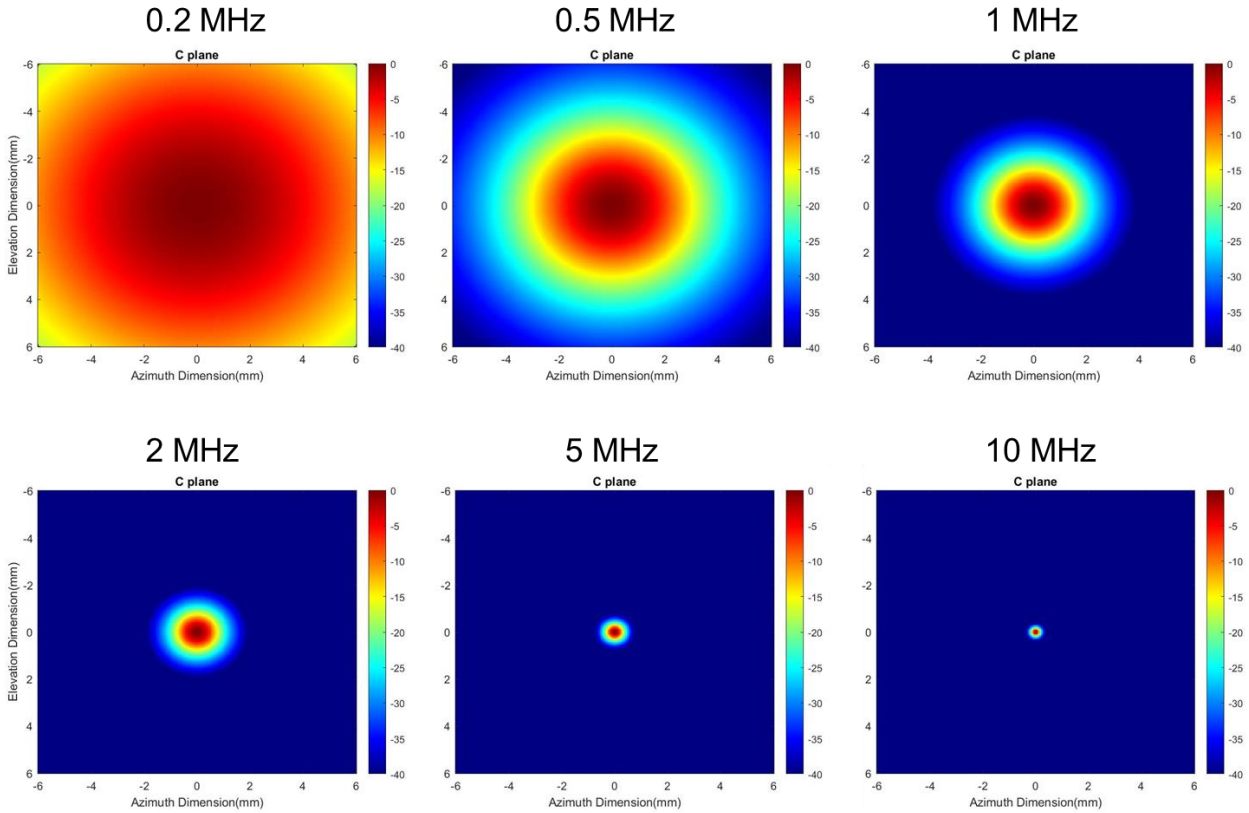

Supplementary Figure 11. The Field II simulation results of the beam width in different frequency (0.2 MHz – 10 MHz) of ultrasound transducer at same focal distance. Under the same ultrasound transducer size, the beam width of the formed acoustic field by Field II simulation is smaller when frequency is increasing [43,44]. For frequency of 0.5 MHz, the beam width is over 3 mm, and the acoustic beam resolution for ultrasound energy transfer is lower. On the other hand, when frequency is over 5 MHz, the acoustic beam width is smaller, but it will have higher attenuation on tissue penetration. Thus, based on the size of piezo-receiver from UIWI stimulator, the diameter of the -6 dB acoustic fields by 1 MHz ultrasound transducer achieved ~1.5 mm which is smaller than the implanted piezo-receiver size, ensuring efficient acoustic energy conversion on the piezo-element during operation.

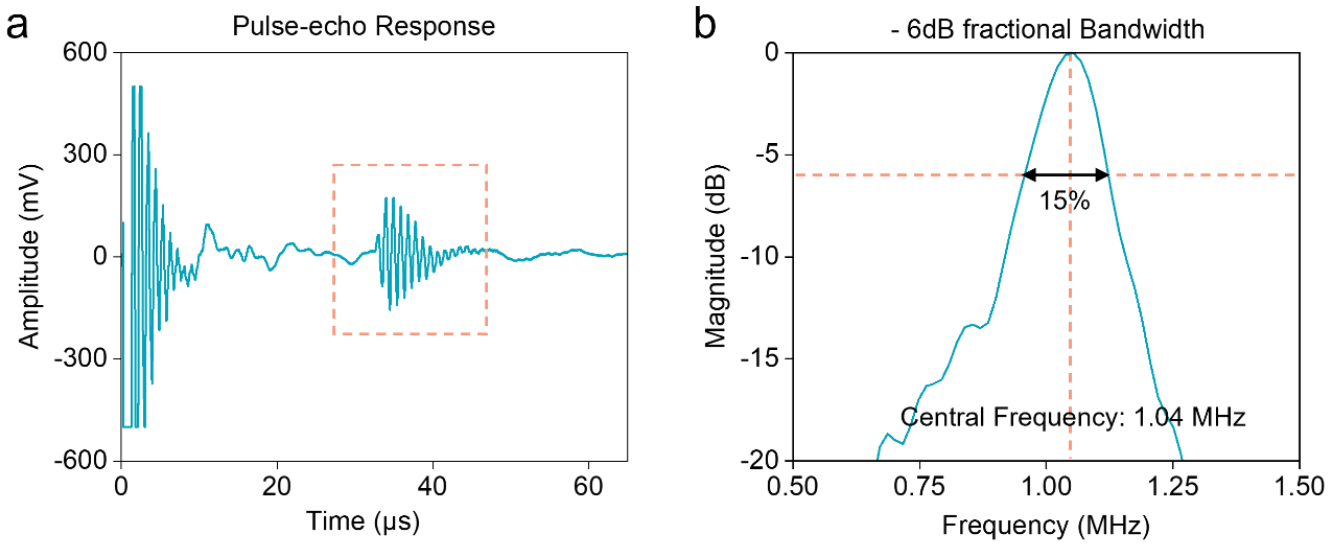

Supplementary Figure 12. Characterization of the WUT in pulse-echo performance. a The measured pulse-echo performance of the WUT. The time located in maximum echo can represent the time in dual way of the ultrasound propagation in the DI-water, calculating the focal distance of the WUT as 25 mm. **b** The FFT spectrum (-6 dB fractional bandwidth) of the pulse-echo response of the WUT. The -6 dB fractional bandwidth, and central frequency of WUT are shown as 15%, and 1.04 MHz, respectively.

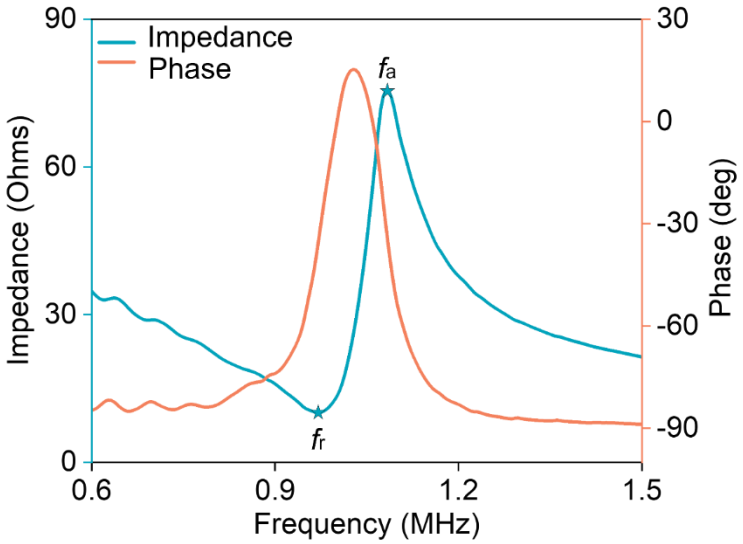

Supplementary Figure 13. Characterization of the WUT in electrical impedance and phase. The resonant frequency (f_r) and anti-resonant frequency (f_a) can be located as 0.95 MHz and 1.08 MHz, respectively. The central frequency is between the f_r and f_a, which is similar to the tested results in Supplementary Fig. 11.

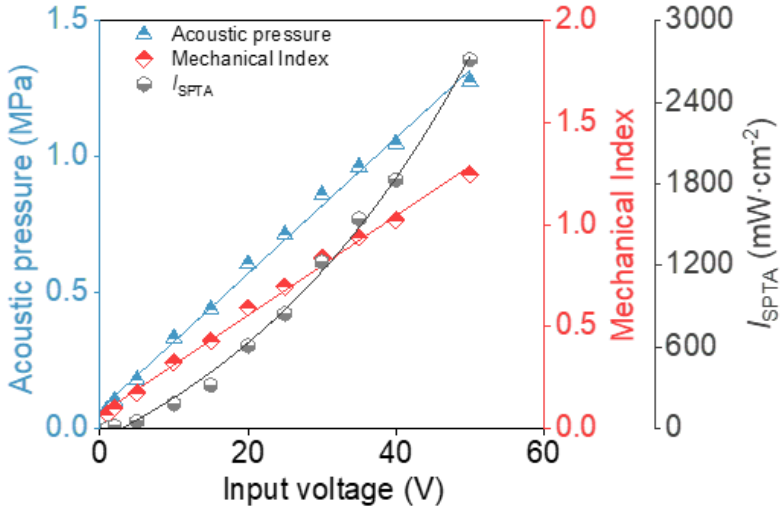

Supplementary Figure 14. Characterization of the WUT with different acoustic intensities. The hydrophone probe was applied to test the acoustic intensity of the WUT. The acoustic pressure, mechanical index, and spatial peak temporal average intensity (I_{spta}) of the WUT are calculated and demonstrated. For further pain management in animal model demonstration, the UIWI stimulator was driven by WUT under input of 1 V, hence, the WUT was working under the U.S. Food and Drug Administration (FDA) regulatory limit on power flux density (I_{spta} <720 mW cm^{-2}, MI <1.9).

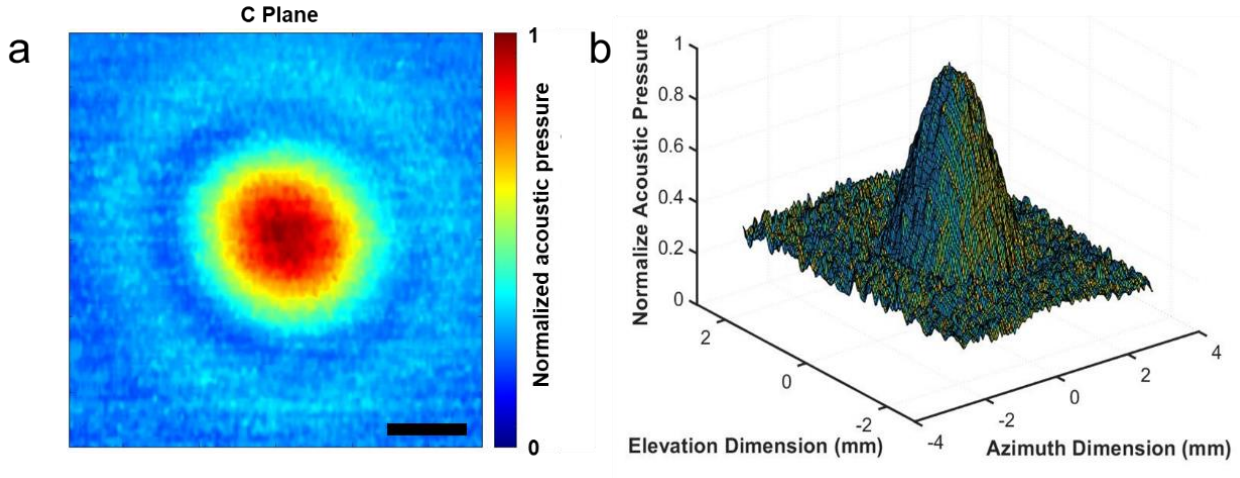

Supplementary Figure 15. Characterization of the WUT in an acoustic field. a Measured 2D-acoustic field in C plane emitted by WUT, exhibiting a symmetrical focused acoustic field. The color bar indicates the normalized acoustic pressure. Scale bar, 1mm. **b** Measured 3D-acoustic field emitted by WUT, showing a spatially confined acoustic field. The results show the -6 dB beamwidth is 1.5 mm in diameter near the focus point, which is below the fabricated piezo-element size of UIWI stimulator in C plane (2 mm × 2 mm).

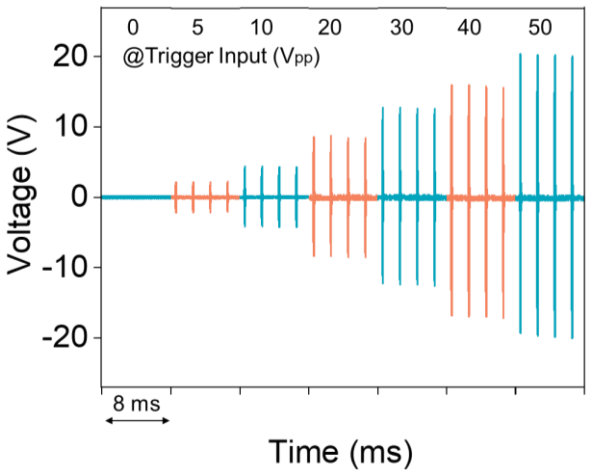

Supplementary Figure 16. Waveforms of unrectified output voltages of UIWI stimulator under different input voltages. WUT driving frequency – 1 MHz, Interval time – 2 ms, Duty cycle – 5 %.

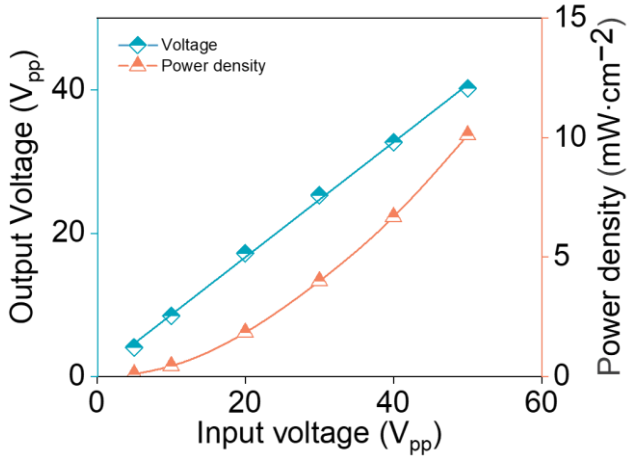

Supplementary Figure 17. Tendency of the unrectified output voltages and the corresponded power density of the UIWI stimulator under different input voltages.

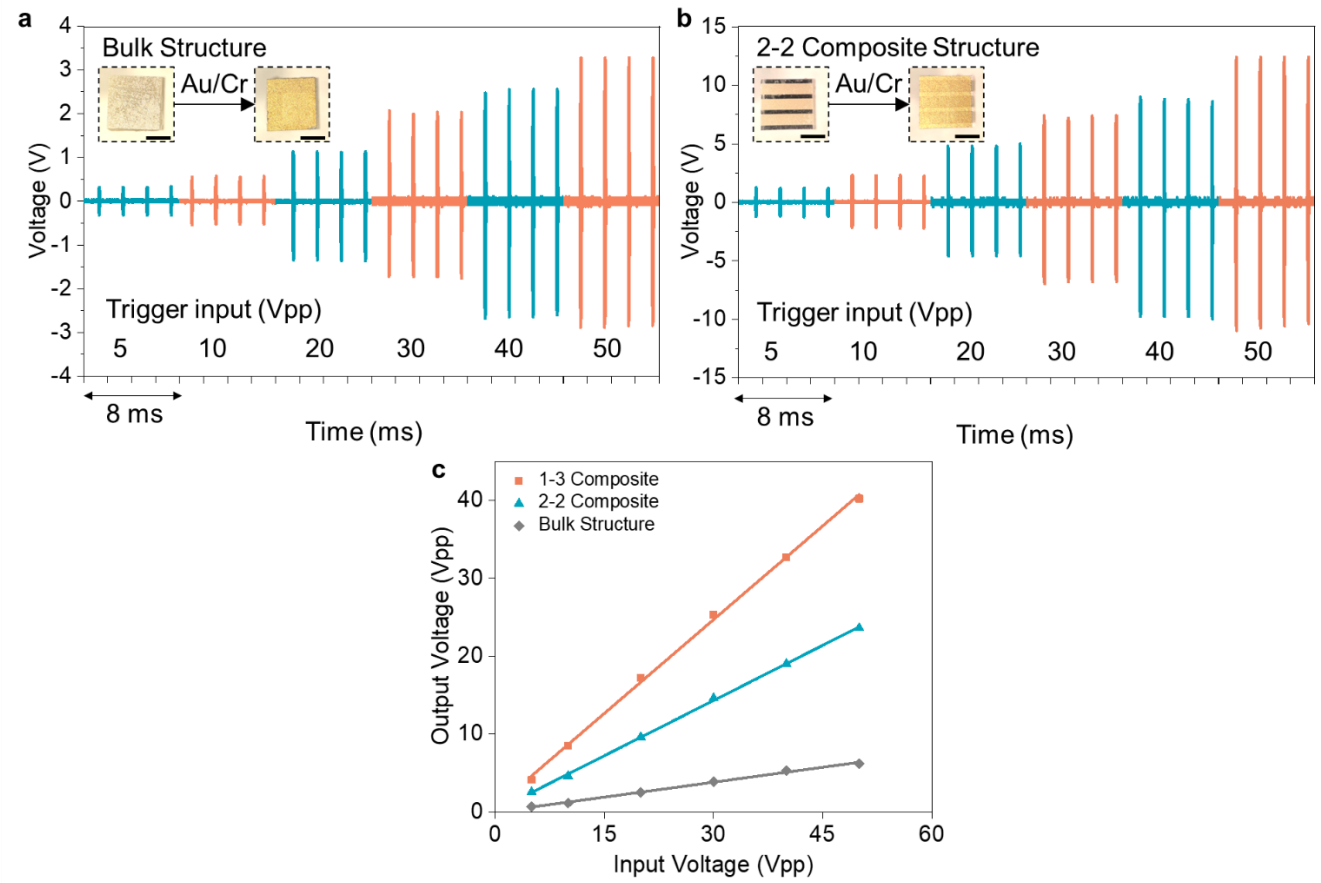

Supplementary Figure 18. Waveforms of unrectified output voltages of **a** bulk structure and **b** 2-2 composite structure under different input voltages. **c** The comparison of unrectified output voltages of the different structures against the triggered input voltage. The results show that 1-3 Composite achieved highest output voltage due to the higher energy transfer efficiency. WUT driving frequency – 1 MHz, Interval time – 2 ms, Duty cycle – 5 %. Scale bar, 1 mm.

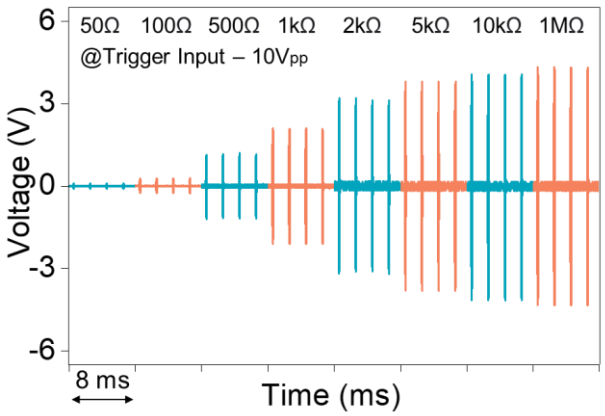

Supplementary Figure 19. Waveforms of the unrectified output voltages of UIWI stimulator under different load resistances. WUT driving frequency – 1 MHz, interval time – 2 ms, duty cycle – 5 %, trigger input voltages – 10 *V*pp. When resistance of the load increases, the output voltage increases progressively at first, and then gradually flattens out under high resistance loads.

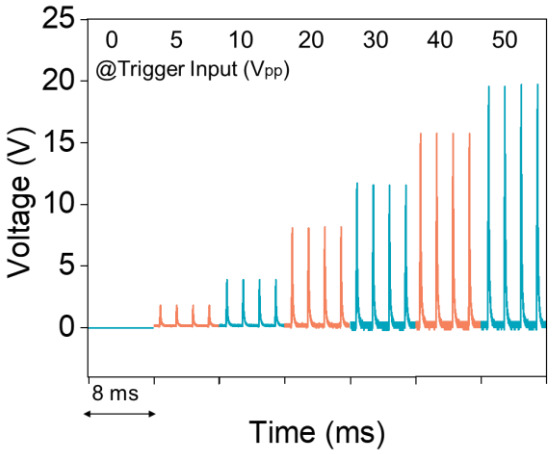

Supplementary Figure 20. Waveforms of the rectified output voltages of UIWI stimulator under different input voltages. WUT driving frequency – 1 MHz, interval time – 2 ms, duty cycle – 5 %.

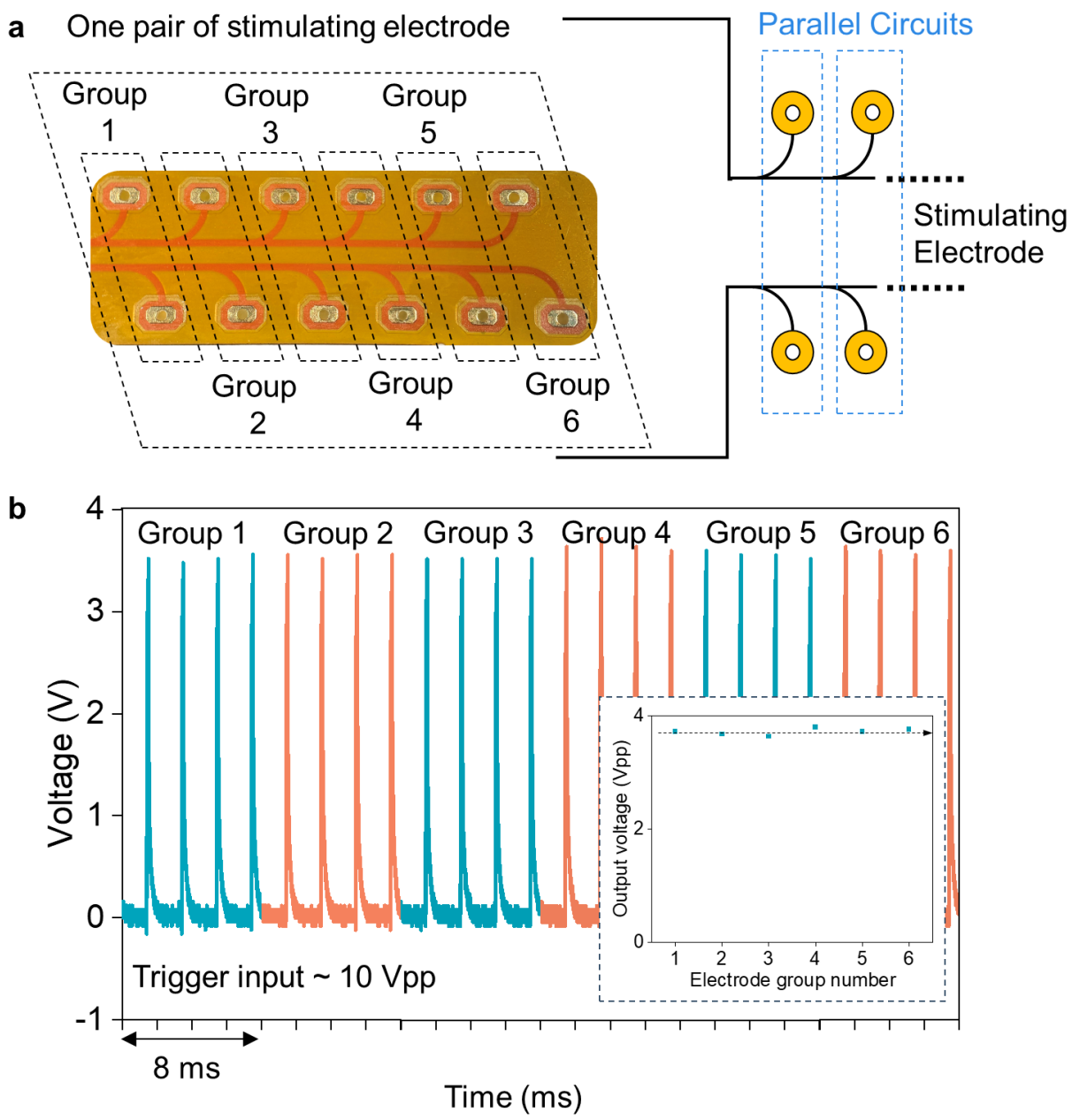

Supplementary Figure 21. Electrodes output measurement. a The details of the UIWI stimulator electrodes. Six sets of electrodes on the two sides. The six electrodes on each side were connected by one copper trace, thus, six sets of electrodes formed one pair of the stimulating electrode on UIWI stimulation device for pain management. **b** The output voltages tested from six sets electrodes. Since six sets of electrodes formed parallel circuits, the output voltages of each set of electrodes are almost the same. WUT driving frequency – 1 MHz, interval time – 2 ms, duty cycle – 5 %.

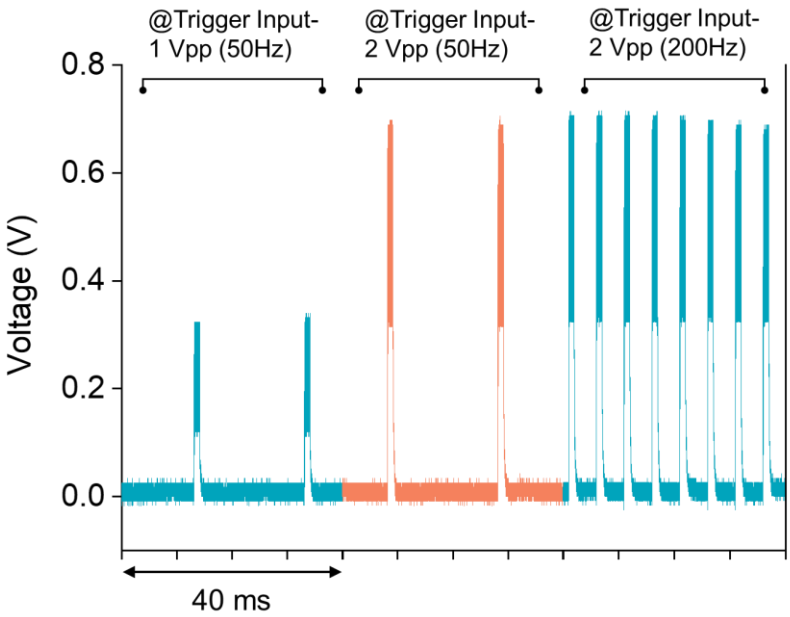

Supplementary Figure 22. Waveforms of rectified output voltages of UIWI stimulator for application of chronic pain management. The interval of the driving WUT has been adjusted for three different pain-symptom level (effective voltage of 199 mV, 20 ms / 50 Hz – slight pain; effective voltage of 409 mV, 20 ms / 50 Hz – moderate pain; effective voltage of 417 mV, 5 ms / 200 Hz – extreme pain). The trigger input was set up as 1 V_{pp} for slight pain management，cycle number: 1000. And the trigger input was set up as 2 V_{pp} for moderate and extreme pain management，cycle number: 1000.

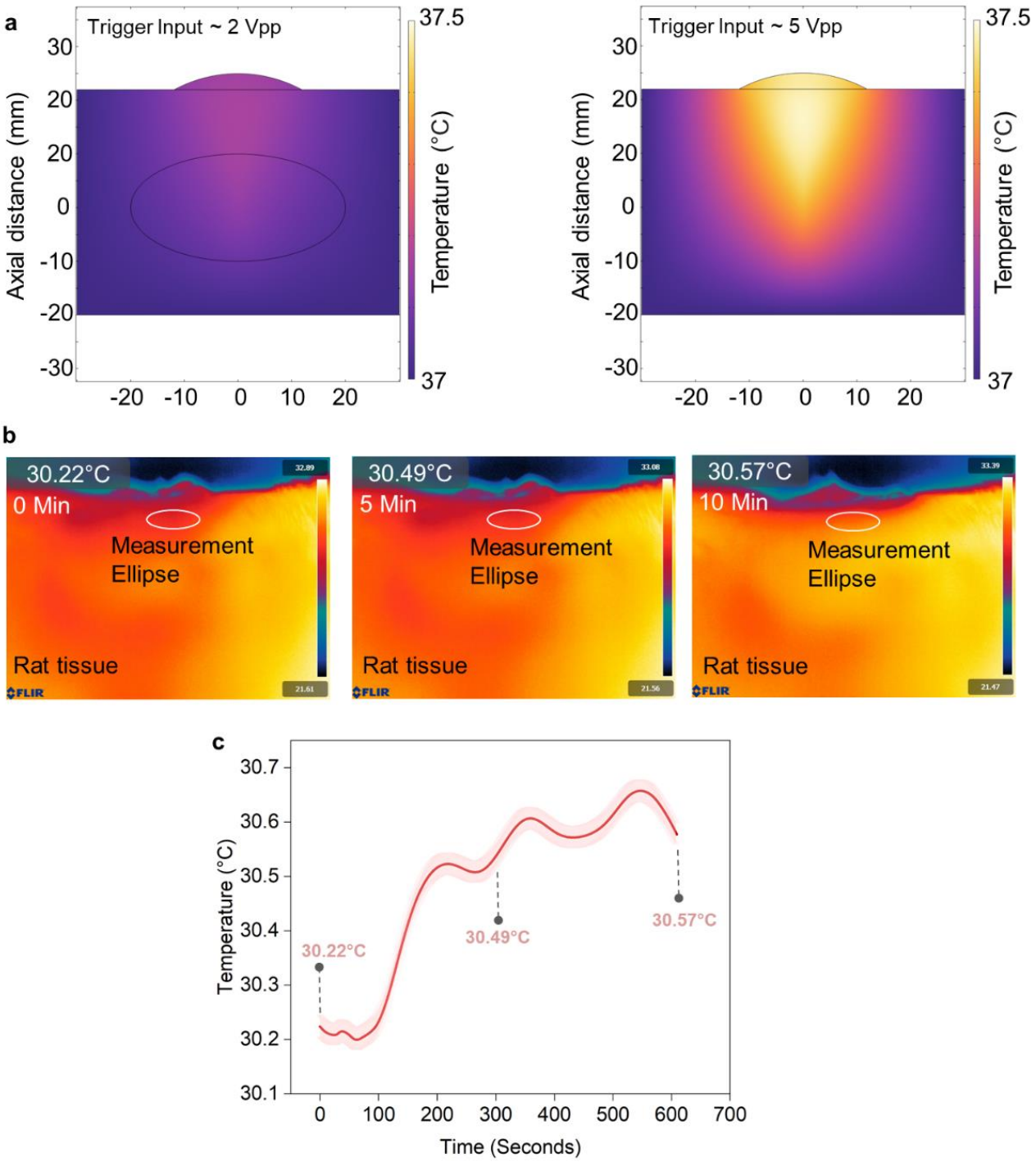

Supplementary Figure 23. Simulation and measurement of the temperature increase on tissue. a FEA simulation results of the temperature increase on tissue. Tissues mainly compose of muscles was assumed and the initial body temperature is 37 °C. Acoustic properties and attenuation in muscles were used in the simulation to mimic the real condition of the tissue [45]. Results show that temperature increase is lower than 0.5 °C when the input voltages are 2 V_{pp} and 5 V_{pp} (our working input voltage in in-vivo test). **b** The infrared camera system (A700 IR temperature measurement system, FLIR LLC, USA) was applied to record the temperature change of the rat back tissue. The WUT was operated under the input voltage of 1 -2 V_{pp} (same

set-up when WUT applied in-vivo for pain-management), and the temperature of the rat back was recorded at 0 min, 5 min, and 10 min. **c** The temperature increasing tendency of the rat back tissue during the use of the WUT. The results indicate that our WUT did not cause substantial temperature change (< 0.5 °C) in tissue when applied in pain-treatment, illustrating the bio-thermally safety of applying our WUT and UIWI stimulator [46]. Data is presented as mean temperatures (solid line) with shaded areas indicating the full range between maximum and minimum temperature values in the measured area.

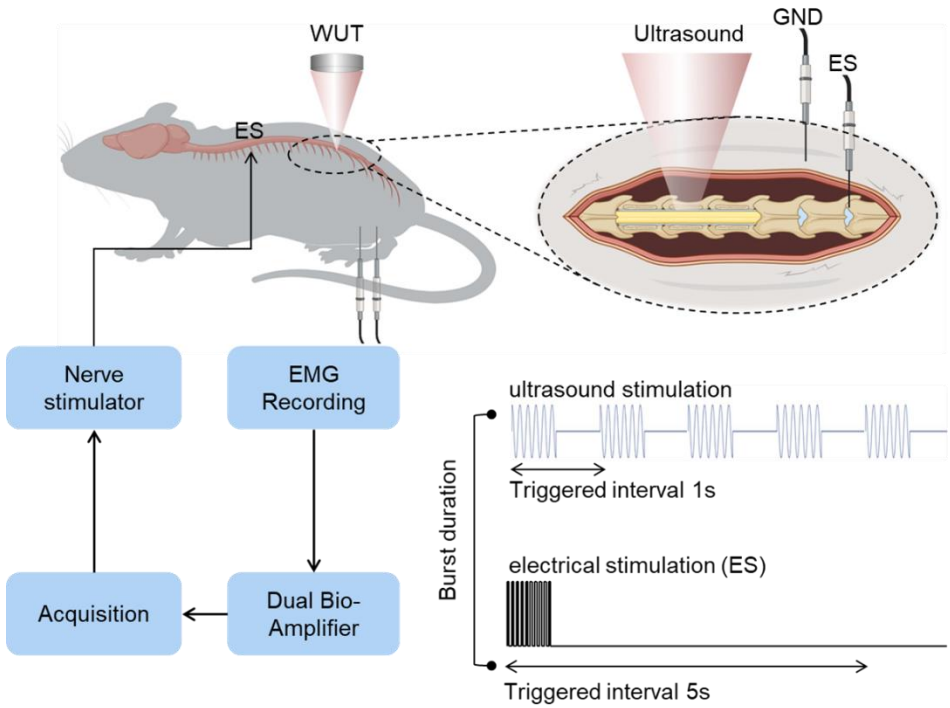

Supplementary Figure 24. The Schematic diagram of the ultrasound stimulation for spinal cord. Set parameters: For electrical stimulation, frequency of 100 Hz and pulses repeated 10 times with 5-second intervals. In contrast, for ultrasound stimulation, shorter 1-second intervals and a burst duration of 300 ms.

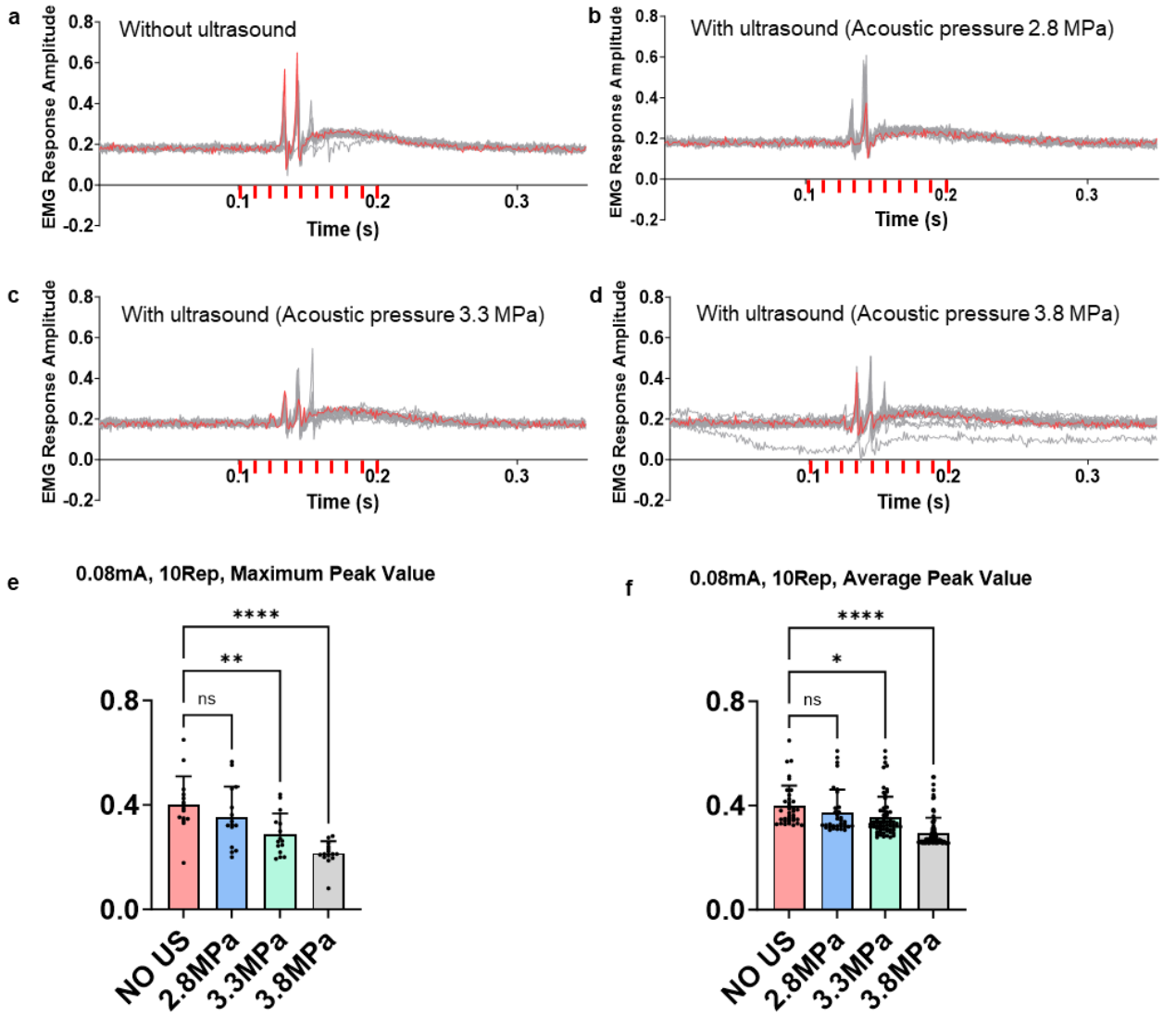

Supplementary Figure 25. Neural response without / with ultrasound stimulation. a – d EMG response amplitude without ultrasound stimulation and with ultrasound (2.8 MPa – 3.8 MPa acoustic intensity). **e** Comparison of maximum peak value without and with ultrasound stimulation. n = 15. p = 0.4069 between NO US and 2.8 MPa, p = 0.0036 between No US and 3.3 MPa, p < 0.0001 between NO US and 3.8 MPa. **f** Comparison of average peak value without and with ultrasound stimulation. n = 36 for NO US, n = 34 for 2.8 MPa group, n = 65 for 3.3 MPa group, n = 92 for 3.8 MPa group. p = 0.4357 between NO US and 2.8 MPa, p = 0.0173 between NO US and 3.3 MPa, p < 0.0001 between NO US and 3.8 MPa. Data is presented as mean ± S.E.M. one-way ANOVA (ns = non-significant, *p < 0.05, **p < 0.01, ****p < 0.0001).

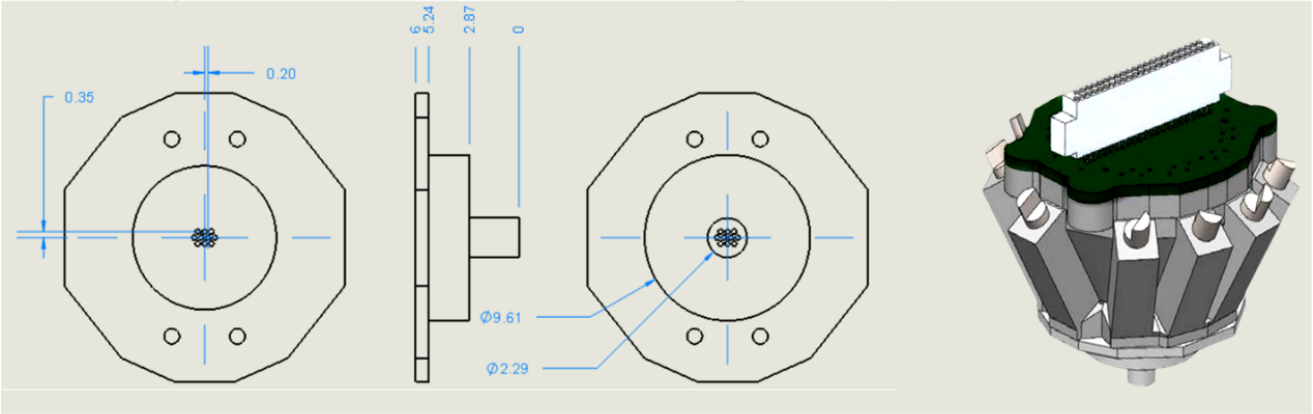

Supplementary Figure 26. Schematic design of the electrodes and a holder for EEG signal recording.

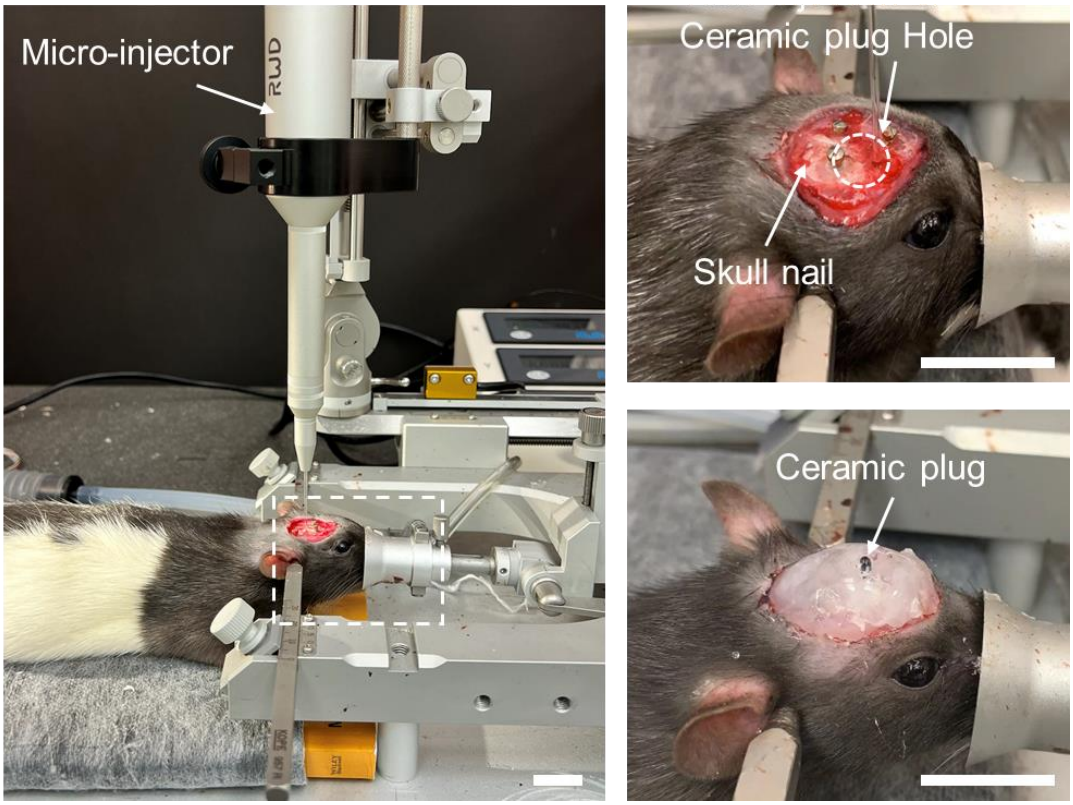

Supplementary Figure 27. Virus injection for fiber photometry. Photometry was applied to verify the classification of the three pain levels (SP, MP, and EP). A 2 mm diameter hole was carefully created above the anterior cingulate cortex of the rat. Using the RWD R-480 microinjector, 0.5 uL of the GCaMP8m (pGP-AAV-syn-jGCaMP8m-WPRE, titer ≥ 1×10^{13} vg/mL, Addgene, USA) virus was injected at anteroposterior (AP) + 2.7 mm, mediolateral (ML) +1.0 mm and dorsoventral (DV) − 2.0 mm. The injection process lasted for 30 min, after which the microinjection needles remained in place for an additional 10 min. The needles were then raised by 1 mm and left for an additional minute to facilitate the diffusion of virus particles away from the injection site while minimizing their spread along the injection tract. A ceramic plug was employed to deliver the excitation light and capture the fluorescence signal. The optical fiber was implanted through the viral injection hole. The fixation of the ceramic plug was achieved using silicon elastomer and dental cement. **Scale bars, 1 cm**.

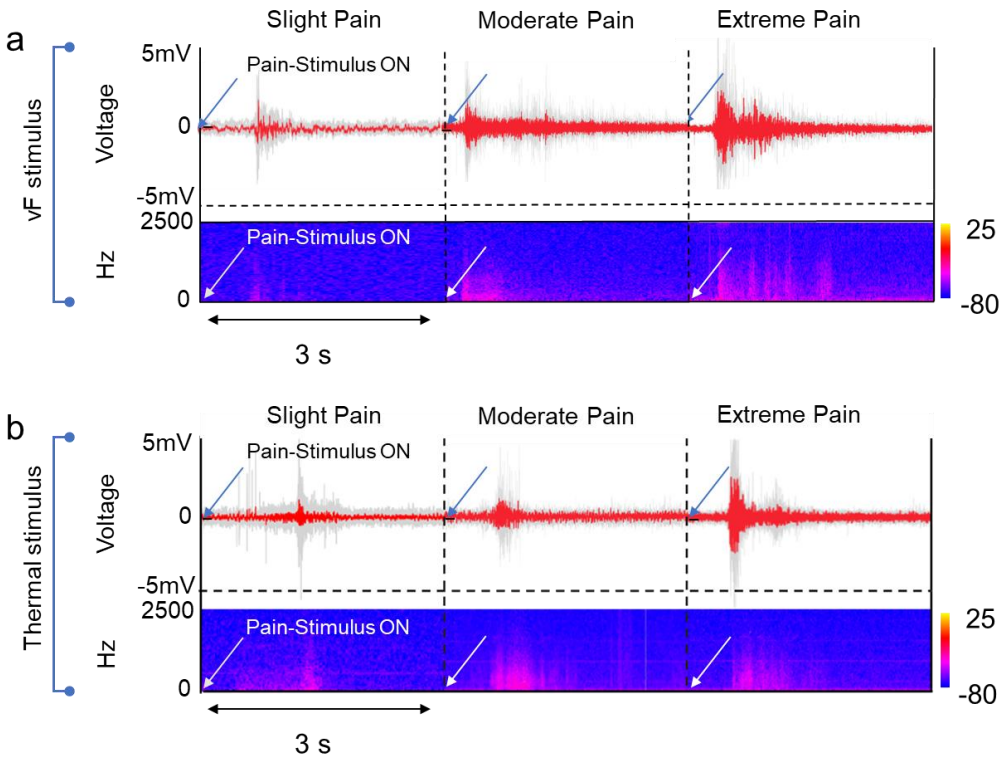

Supplementary Figure 28. The electrophysiological responses and spectral representations of the anterior cingulate cortex (ACC) to pain stimuli. The electrophysiological signals from the ACC under various stimulus conditions is represented. **a** the neuron response of the vF stimuli (Slight, Moderate & Extreme Pain), along with the corresponding spectral views. **b** the neuron response and spectral views to three types of laser thermal stimuli. The arrows represent the start time of the stimuli.

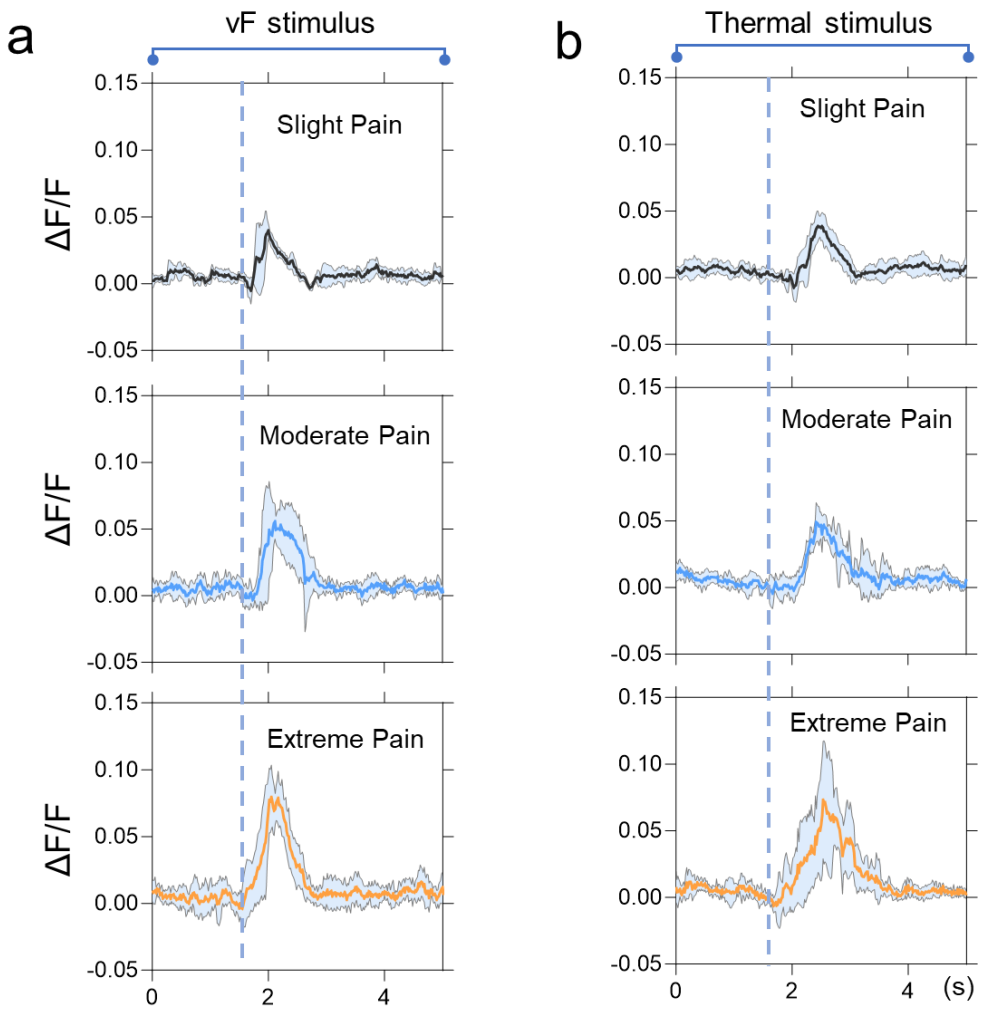

Supplementary Figure 29. The results of fiber-optic calcium imaging of the anterior cingulate cortex (ACC) in response to pain stimuli. a The neuron responses to three types of the vF stimuli (Slight, Moderate & Extreme Pain), **b** The neuron responses to three types of laser thermal stimuli. The dotted line represents the start time of stimulus. The light trace represents the estimated Z-score from the univariate latent state, and the shaded area denotes the 95% confidence interval. The ceramic plug was used to deliver the excitation light and collect fluorescence signal. The fiber photometry system (Neuroscience Console 500, Integrated Flourance Mini Gen3, Doric Lenses, Canada) was used to emit the 470 nm excitation light and collect the fluorescence signal, selectively capturing the response from the ACC.

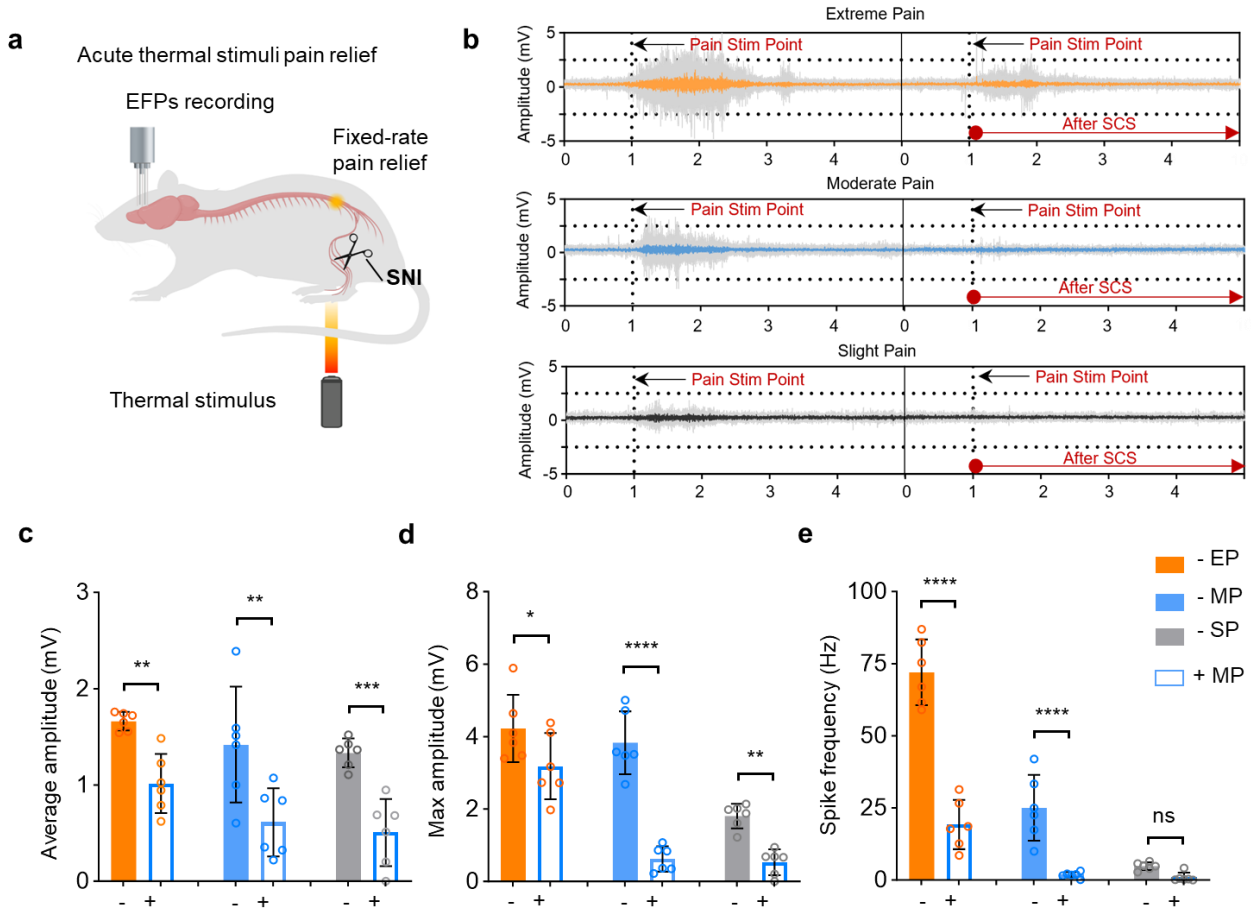

Supplementary Figure 30. Thermal stimulation pain management experiment by fixed-rate pain management. a Schematic representation of chronic neuropathic pain management model with fixed-rate stimulation. **b** Neural response to evoked pain stimuli captured by the EFPs signals pre- and post- fixed-rate SCS treatment. The light gray trace represents the 4 groups of the trails while the highlighted trail was the fifth experimental result. **c** Comparison of average amplitude of the EFP signal of evoked pain models before and after ultrasound-induced fixed-rate SCS treatment. n = 6. **p = 0.0098 between - EP and + MP, **p = 0.0012 between -MP and + MP, ***p = 0.0009 between - SP and + MP. **d** Comparison of max filtered spikes' amplitude before and after fixed-rate SCS treatment on evoked pain models. n =6. *p = 0.039 between - EP and + MP, ****p < 0.0001 between -MP and + MP, **p = 0.009 between - SP and + MP. **e** Comparison of spike frequency before and after fixed-rate SCS treatment on evoked pain models. n = 6. ****p < 0.0001 between - EP and + MP, ****p < 0.0001 between -MP and + MP, ns p = 0.76 between - SP and + MP. Data is presented as mean ± S.E.M. one-way ANOVA.

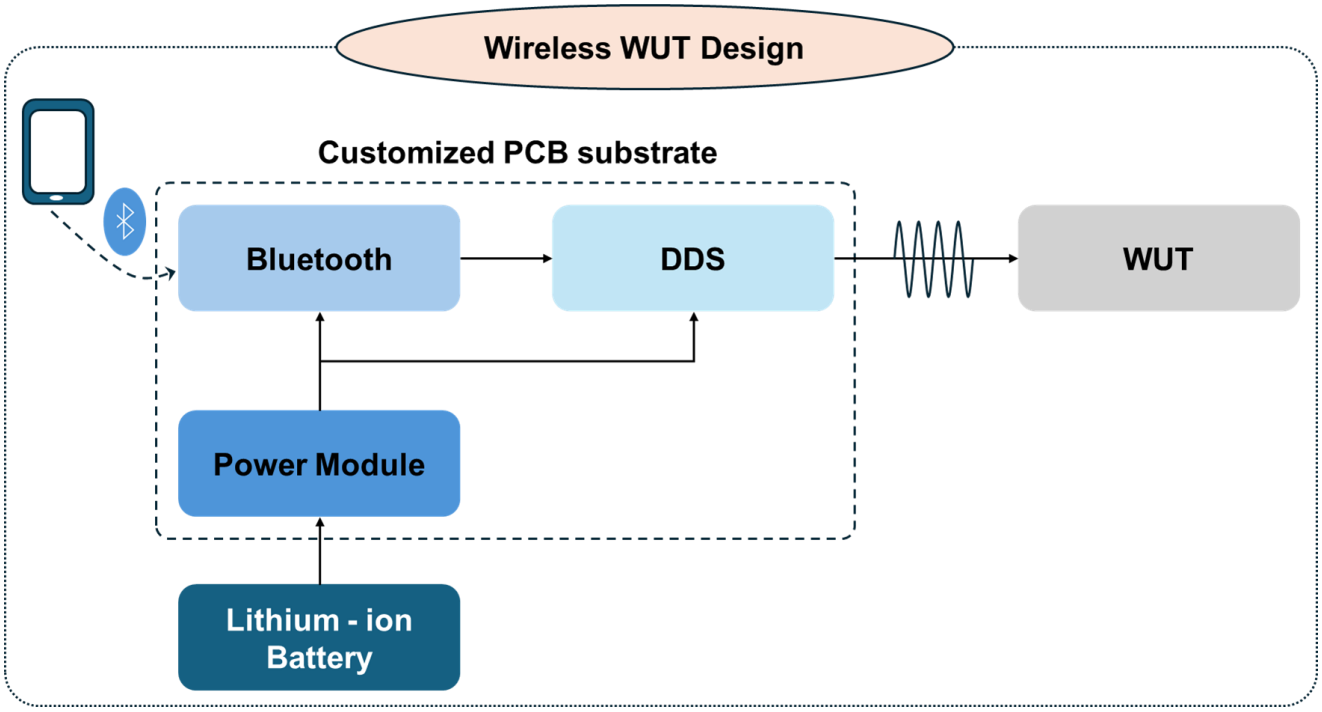

Supplementary Figure 31. The future design of the WUT with wireless driving system. DDS, Direct Digital Synthesis. WUT, Wearable Ultrasound Transmitter.

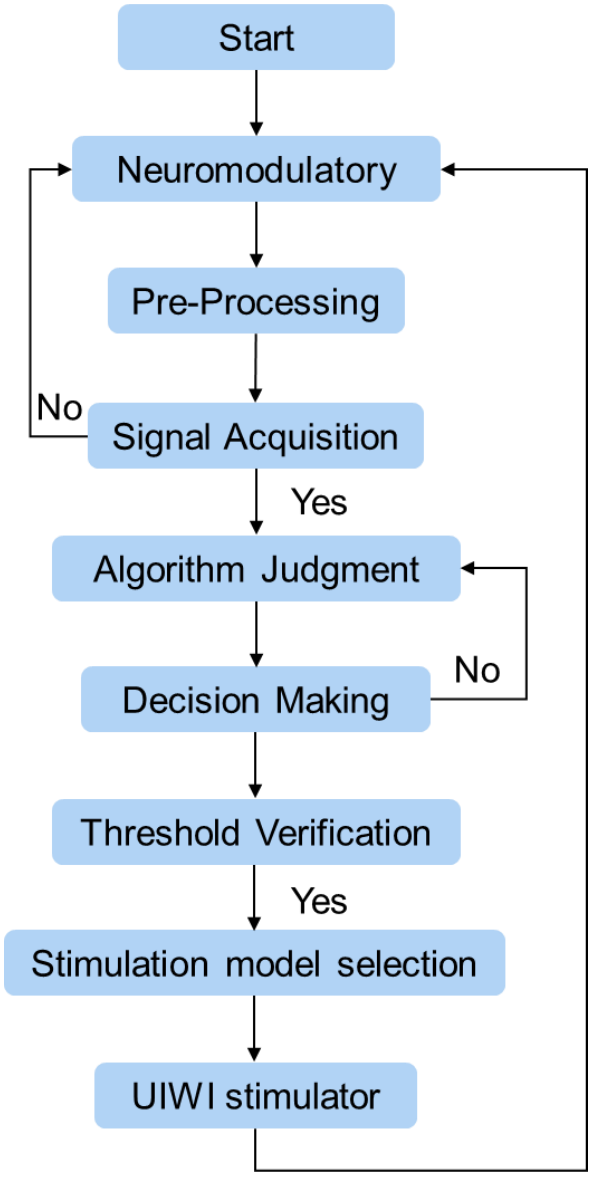

Supplementary Figure 32. Feedback loop of chronic neuropathic pain management model. In the study, the machine-learning model classifies the different pain level based on the neural recordings, then different pain-level was corresponded to the specific electrical stimulation modes from our proposed device and system. Since our system is closed-loop, it performs real-time pain detection continuously while administering electrical stimulation therapy. If misclassification occurs, and the pain signal is still be detected after this wrongly-classified electrical stimulation, our system will automatically provide next feedback quickly to correct the wrongly-classified electrical stimulation.

Supplementary Table 1. Features of the currently wireless energy transfer technologies.

	Ultrasound Wave	EM wave
Wave velocity	1500 m/s	3×10^{8} m/s
Wavelength	μm level	mm level
Commonly used Frequency	1 – 10 MHz	2 GHz – 10 GHz
Attenuation	0.5 – 1 dB cm^{-1} (~2 MHz)	10 – 12 dB cm^{-1} (~2 GHz)
Power efficiency	2% - 20%	1 % - 29%
Medium	Required	None
FDA limited power flux density	720 mW/cm^{2}	10 mW/cm^{2}
Ref	[3,46-58]	

Supplementary Table 2. Comparison between our work and other representative stimulus works for pain management.

	Ref[59]	Ref[60]	Ref[61]	Ref[62]	Our Work
Type	Electrical	Cooling	Electrical/ Light	Optogenetic	Electrical
Link	Waveform Generator	liquid coolant	AC / IR	Blue laser	Ultrasound
Stimulus location	peroneal nerve	sciatic nerve	Unmyelinated nerves	Brain	Spina cord
stimulus parameter	2-10 V	0 - 5℃	10 - 15 mA 0.177 - 0.254 J/cm^2	20 Hz pulse-width	200 - 450 mV
Implantable	Yes	Yes	Yes	Yes	Yes
Animal model	Mice	Rat	Aplysia	Rat	Rat
Connection	Wire-based	Wire-based	Wire/fiber-based	Wire-based	Wireless

Supplementary Table 3. Parameters of the materials

Parameters	Raw PZT-5H ceramic (PZT DL-53, Del-piezo Specialties, LLC, USA)	Fabricated PZT 1-3 Composite (This Work)
d_{33} (pC/N)	730	670
k_t	0.49	0.63
$\varepsilon_{33}^T/\varepsilon_0$ (under 1 KHz)	3350	1909
g_{33} (Vm/N × 10^{-3})	25.6	41
ρ (g/cm^3)	7.6	4.75
PZT Volume fraction	100%	56.2%

d_{33}: Piezoelectrical coefficient.

k_t: Electromechanical coupling coefficient.

$\varepsilon_{33}^T/\varepsilon_0$: Dielectric Constant.

g_{33}: Piezoelectric voltage coefficient.

ρ: Density.

Supplementary Table 4. Acoustic pressure, intensity, and MI under different input voltage of the WUT

Input Voltage (V_{pp})	Acoustic pressure (MPa)	MI	I_{spta} (mw.cm^{-2})
1	0.071	0.070	1.718
2	0.103	0.101	17.85
5	0.179	0.174	53.40
10	0.332	0.324	184.0
15	0.438	0.428	321.1
20	0.605	0.590	610.8
25	0.712	0.695	845.4
30	0.857	0.837	1226.7
35	0.961	0.938	1541.5
40	1.047	1.022	1828.4
50	1.275	1.245	2713.4

Mechanical Index (MI).

Wearable ultrasound transmitter (WUT).

Spatial-peak temporal average (I_{spta}).

Supplementary Table 5. Applied machine leaning models' comparison

Model name (number of iterations, mini batch size)	Accuracy (%)	Error counter	Training time (min or s)	Test time (s)
ResNet18(10,256)	97.66	12	23s	1.2
ResNet18(20,256)	99.73	1	46s	1.2
ResNet18(30,256)	99.73	1	46s	1.15
ResNet18(10,128)	98.03	11	45s	1.18
ResNet18(20,128)	98.71	9	1min24s	1.13
ResNet18(30,128)	97.94	24	2min6s	1.23
ResNet18(10,64)	94.64	42	1min23s	6.67
ResNet18(20,64)	99.59	1	2min50s	1.18
ResNet18(30,64)	99.58	3	4min18s	1.13
ResNet50(10,256)	99.59	0	1min16s	2.6
ResNet50(20,256)	100	0	2min23s	2.45
ResNet50(30,256)	100	0	3min36s	2.34
ResNet50(10,128)	96.58	46	2min7s	2.52
ResNet50(20,128)	100	0	4min3s	2.38
ResNet50(30,128)	99.72	4	6min25s	2.5
ResNet50(10,64)	80.88	121	4min11s	2.16
ResNet50(20,64)	99.33	4	8min1s	2.49
ResNet50(30,64)	99.72	0	12min18s	2.43
ResNet101(10,256)	75.73	206	2min36s	8.61
ResNet101(20,256)	97.98	11	5min26s	4.46
ResNet101(30,256)	99.97	0	7min28s	4.48
ResNet101(10,128)	91.41	49	4min46s	9.37
ResNet101(20,128)	48.76	388	9min22s	8.55
ResNet101(30,128)	99.69	1	14min3s	9.07
ResNet101(10,64)	36.18	570	9min38s	5.43
ResNet101(20,64)	3.64	1621	18min55s	6.85
ResNet101(30,64)	87.93	76	28min13s	7.88
DarkNet19(10,256)	12.72	1315	31s	1.46
DarkNet19(20,256)	49.27	290	47s	1.55
DarkNet19(30,256)	49.27	290	47s	1.41
DarkNet19(10,128)	3.06	2605	48s	1.57
DarkNet19(20,128)	2.38	1463	1min27s	1.47
DarkNet19(30,128)	53.62	291	2min5s	1.52
DarkNet19(10,64)	2.12	2692	1min36s	1.35
DarkNet19(20,64)	1.93	1997	3min	1.52
DarkNet19(30,64)	2.15	3087	4min23s	1.45
DarkNet53(10,256)	63.05	377	1min29s	2.84
DarkNet53(20,256)	3.08	1905	2min36s	3.16

DarkNet53(30,256)	87.84	91	3min52s	2.98
DarkNet53(10,128)	1.1	3311	2min40s	2.68
DarkNet53(20,128)	43.82	598	5min10s	2.7
DarkNet53(30,128)	47.98	716	7min41s	2.68
DarkNet53(10,64)	53.84	1596	5min34s	2.65
DarkNet53(20,64)	16.43	2364	11min7s	2.65
DarkNet53(30,64)	55.49	1511	16min3s	2.78

Supplementary References

1 Hinchet, R. *et al.* Transcutaneous ultrasound energy harvesting using capacitive triboelectric technology. *Science* **365**, 491-494 (2019).

2 Kim, T. *et al.* Deep brain stimulation by blood–brain-barrier-crossing piezoelectric nanoparticles generating current and nitric oxide under focused ultrasound. *Nat. Biomed. Eng.* **7**, 149-163 (2023).

3 Zeng, Y. *et al.* 3D-printing piezoelectric composite with honeycomb structure for ultrasonic devices. *Micromachines.* **11**, 713 (2020).

4 Kwok, K. W., Chan, H. L. W. & Choy, C. L. Evaluation of the material parameters of piezoelectric materials by various methods. *IEEE Trans. Ultrason, Ferroelectr. Freq. Control.* **44**, 733-742 (1997).

5 Meeker, T. Publication and proposed revision of ANSI/IEEE standard 176-1987. *IEEE Trans. Ultrason, Ferroelectr. Freq. Control.* **43**, 717-772 (1996).

6 Boehler, C., Carli, S., Fadiga, L., Stieglitz, T. & Asplund, M. Tutorial: guidelines for standardized performance tests for electrodes intended for neural interfaces and bioelectronics. *Nat. Protoc.* **15**, 3557-3578 (2020).

7 Gong, Y. *et al.* Stability performance analysis of various packaging materials and coating strategies for chronic neural implants under accelerated, reactive aging tests. *Micromachines* **11**, 810 (2020).

8 Cen-Puc, M., Schander, A., Vargas Gleason, M. G. & Lang, W. An assessment of surface treatments for adhesion of polyimide thin films. *Polymers* **13**, 1955 (2021).

9 Kuliasha, C. A. & Judy, J. W. The Materials Science Foundation supporting the microfabrication of reliable polyimide–metal neuroelectronic interfaces. *Adv. Mater. Tech.* **6**, 2100149 (2021).

10 Xiao, D., Fan, Q., Xu, C. & Zhang, X. Measurement methods of ultrasonic transducer sensitivity. *Ultrasonics.* **68**, 150-154 (2016).

11 Shung, K. K. & Zippuro, M. Ultrasonic transducers and arrays. *IEEE Eng. Med. Biol. Mag.* **15**, 20-30 (1996).

12 Radulescu, E. G., Lewin, P. A., Goldstein, A. & Nowicki, A. Hydrophone spatial averaging corrections from 1 to 40 MHz. *IEEE Trans. Ultrason, Ferroelectr. Freq. Control.* **48**, 1575-1580 (2001).

13 Schafer, M. E., Ziskin, M. & Lewin, P. The angular spectrum method of transducer characterization. *Ultrasonic exposimetry* 216-255 (CRC Press Boca Raton, FL, 1993).

14 Şen, T., Tüfekçioğlu, O. & Koza, Y. Mechanical index. *Anatol J. Cardiol.* **15**, 334 (2015).

15 Shi, Q., Wang, T. & Lee, C. MEMS based broadband piezoelectric ultrasonic energy harvester (PUEH) for enabling self-powered implantable biomedical devices. *Sci. Rep.* **6**, 24946 (2016).

16 Dreibati, B., Lavet, C., Pinti, A. & Poumarat, G. Influence of electrical stimulation frequency on skeletal muscle force and fatigue. *Ann. Phys. Rehabil. Med.* **53**, 266-277 (2010).

17 Pantaleão, M. A. *et al.* Adjusting pulse amplitude during transcutaneous electrical nerve stimulation (TENS) application produces greater hypoalgesia. *J. Pain* **12**, 581-590 (2011).
18 Payne, A. H. *et al.* Magnetic resonance imaging-guided focused ultrasound to increase localized blood-spinal cord barrier permeability. *Neural regener.Res.* **12**, 2045-2049 (2017).
19 Fletcher, S.-M. P., Choi, M., Ramesh, R. & O'Reilly, M. A. Focused ultrasound-induced blood–spinal cord barrier opening using short-burst phase-keying exposures in rats: A parameter study. *Ultrason. Med. Biol.* **47**, 1747-1760 (2021).
20 Tsehay, Y. *et al.* Low-intensity pulsed ultrasound neuromodulation of a rodent's spinal cord suppresses motor evoked potentials. *IEEE Trans. Biomed. Eng.* (2023).
21 Liao, Y.-H. *et al.* Effects of noninvasive low-intensity focus ultrasound neuromodulation on spinal cord neurocircuits in vivo. *Evi-Based Complement. Altern. Med.* **2021** (2021).
22 Aljalal, M., Aldosari, S. A., Molinas, M., AlSharabi, K. & Alturki, F. A. Detection of Parkinson's disease from EEG signals using discrete wavelet transform, different entropy measures, and machine learning techniques. *Sci. Rep.* **12**, 22547 (2022).
23 Murphy, N. *et al.* Neural complexity EEG biomarkers of rapid and post-rapid ketamine effects in late-life treatment-resistant depression: a randomized control trial. *Neuropsychopharmacol.* 1-8 (2023).
24 Costa, M., Goldberger, A. L. & Peng, C.-K. Multiscale entropy analysis of biological signals. *Phys. Rev. E* **71**, 021906 (2005).
25 Herzog, L. E. *et al.* Mouse mutants in schizophrenia risk genes GRIN2A and AKAP11 show EEG abnormalities in common with schizophrenia patients. *Transl. Psych.* **13**, 92 (2023).
26 Ahmad, J. *et al.* From mechanisms to markers: novel noninvasive EEG proxy markers of the neural excitation and inhibition system in humans. *Transl. Psych.* **12**, 467 (2022).
27 Cao, Z. & Lin, C.-T. Inherent fuzzy entropy for the improvement of EEG complexity evaluation. *IEEE Trans. Fuzzy Sys.* **26**, 1032-1035 (2017).
28 Ocak, H. Automatic detection of epileptic seizures in EEG using discrete wavelet transform and approximate entropy. *Exp. Sys. Applic.* **36**, 2027-2036 (2009).
29 Montesinos, L., Castaldo, R. & Pecchia, L. On the use of approximate entropy and sample entropy with centre of pressure time-series. *J. Neuroeng. Rehabil.* **15**, 1-15 (2018).
30 Kaffashi, F., Foglyano, R., Wilson, C. G. & Loparo, K. A. The effect of time delay on approximate & sample entropy calculations. *Physica D: Nonlin. Phenom.* **237**, 3069-3074 (2008).
31 Song, Z., Ultenius, C., Meyerson, B. A. & Linderoth, B. Pain relief by spinal cord stimulation involves serotonergic mechanisms: an experimental study in a rat model of mononeuropathy. *Pain.* **147**, 241-248 (2009).
32 Schechtmann, G., Wallin, J., Meyerson, B. A. & Linderoth, B. Intrathecal clonidine potentiates suppression of tactile hypersensitivity by spinal cord stimulation in a model of neuropathy. *Anesth. Analg.* **99**, 135-139 (2004).

33 Wang, J. *et al.* A microstructure engineered perovskite super anode with Li-storage life of exceeding 10,000 cycles. *Nano Energy* **94**, 106972 (2022).

34 Licht, S., Cui, B., Stuart, J., Wang, B. & Lau, J. Molten air–a new, highest energy class of rechargeable batteries. *Energy & Environ. Sci.* **6**, 3646-3657 (2013).

35 Wang, C.-Y. *et al.* Fast charging of energy-dense lithium-ion batteries. *Nature* **611**, 485-490 (2022).

36 Zhou, G., Chen, H. & Cui, Y. Formulating energy density for designing practical lithium–sulfur batteries. *Nat. Energy* **7**, 312-319 (2022).

37 Cao, W., Zhang, J. & Li, H. Batteries with high theoretical energy densities. *Energy Storage Mater.* **26**, 46-55 (2020).

38 Cairns, E. J. Batteries, overview. *Encycl. Energy* **1**, 117-126 (2004).

39 Landi, B. J., Cress, C. D. & Raffaelle, R. P. High energy density lithium-ion batteries with carbon nanotube anodes. *J. Mater. Res.* **25**, 1636-1644 (2010).

40 Zhou, Y. *et al.* Giant magnetoelastic effect in soft systems for bioelectronics. *Nat. Mater.* **20**, 1670-1676 (2021).

41 Zhao, X. *et al.* Permanent fluidic magnets for liquid bioelectronics. *Nat. Mater.* 1-8 (2024).

42 Zhao, X. *et al.* A self-filtering liquid acoustic sensor for voice recognition. *Nat. Electron.* 1-9 (2024).

43 Jensen, J. A. & Svendsen, N. B. Calculation of pressure fields from arbitrarily shaped, apodized, and excited ultrasound transducers. *IEEE Trans. Ultrason, Ferroelectr, Freq. Control* **39**, 262-267 (1992).

44 Jensen, J. A. Field: A program for simulating ultrasound systems. *Med. Biol. Eng. Comput.* **34**, 351-353 (1997).

45 Nassiri, D., Nicholas, D. & Hill, C. Attenuation of ultrasound in skeletal muscle. *Ultrasonics* **17**, 230-232 (1979).

46 Jiang, L. *et al.* Flexible ultrasound-induced retinal stimulating piezo-arrays for biomimetic visual prostheses. *Nat. Comm.* **13**, 3853 (2022).

47 Li, Y. *et al.* Co-evaluation of reflection loss and surface wave attenuation for magnetic absorbing material. *IEEE Trans. Antennas. Propag.* **66**, 6057-6060 (2018).

48 Varotto, G. & Staderini, E. A 2D simple attenuation model for EM waves in human tissues: Comparison with a FDTD 3D simulator for UWB medical radar. in *2008 IEEE Inter Conf. ultra-wideband.* 1-4 (IEEE).

49 Madsen, E. L., Zagzebski, J. A., Banjavie, R. A. & Jutila, R. E. Tissue mimicking materials for ultrasound phantoms. *Med. Phys.* **5**, 391-394 (1978).

50 Shi, C. *et al.* Application of a sub–0.1-mm3 implantable mote for in vivo real-time wireless temperature sensing. *Sci. Adv.* **7**, eabf6312 (2021).

51 Akoev, G., Avelev, V. & Semenjkov, P. Reception of low-intensity millimeter-wave electromagnetic radiation by the electroreceptors in skates. *Neurosci.* **66**, 15-17 (1995).

52 Sonmezoglu, S., Fineman, J. R., Maltepe, E. & Maharbiz, M. M. Monitoring deep-tissue oxygenation with a millimeter-scale ultrasonic implant. *Nat. Biotech.* **39**, 855-864 (2021).

53 Aslan, E. E. Electromagnetic radiation survey meter. *IEEE Trans. Instrum. Meas.* **19**, 368-372 (1970).
54 Chen, Y. *et al.* Energy harvesting and wireless power transmission by a hybridized electromagnetic–triboelectric nanogenerator. *Energy & Environ. Sci.* **12**, 2678-2684 (2019).
55 McSpadden, J. O., Fan, L. & Chang, K. Design and experiments of a high-conversion-efficiency 5.8-GHz rectenna. *IEEE Trans. Microw. Theory. Tech.* **46**, 2053-2060 (1998).
56 Jiang, L. *et al.* Flexible lead-free piezoelectric arrays for high-efficiency wireless ultrasonic energy transfer and communication. *Mater. Horiz.* **9**, 2180-2190 (2022).
57 Nikolayev, D., Zhadobov, M., Karban, P. & Sauleau, R. Electromagnetic radiation efficiency of body-implanted devices. *Phys. Rev. Appl.* **9**, 024033 (2018).
58 Agarwal, K. & Guo, Y.-X. Interaction of electromagnetic waves with humans in wearable and biomedical implant antennas. in *2015 Asia-Pacific Symp Electromag Compat (APEMC).* 154-157 (IEEE).
59 Lee, G. *et al.* A bioresorbable peripheral nerve stimulator for electronic pain block. *Sci. Adv.* **8**, eabp9169 (2022).
60 Reeder, J. T. *et al.* Soft, bioresorbable coolers for reversible conduction block of peripheral nerves. *Science* **377**, 109-115 (2022).
61 Lothet, E. H. *et al.* Alternating current and infrared produce an onset-free reversible nerve block. *Neurophoton.* **1**, 011010-011010 (2014).
62 Ji, Y.-W. *et al.* Plasticity in ventral pallidal cholinergic neuron-derived circuits contributes to comorbid chronic pain-like and depression-like behaviour in male mice. *Nat. Comm.* **14**, 2182 (2023).